Enhanced hydrological cycling and continental weathering during the Jenkyns Event in a lake system in the Sichuan Basin, China

Renping Liu [a], Guang Hu [a,*], Jian Cao [b], Ruofei Yang [c], Zhiwei Liao [d], Chaowei Hu [a], Qian Pang [a], Peng Pang [a]

[a] Natural Gas Geology Key Laboratory of Sichuan Province, Southwest Petroleum University, Chengdu 610500, China
[b] School of Earth Sciences and Engineering, Nanjing University, Nanjing 210023, China
[c] State Key Laboratory of Ore Deposit Geochemistry, Institute of Geochemistry, Chinese Academy of Sciences, Guiyang 550081, China
[d] State Key Laboratory of Coal Mine Disaster Dynamics and Control, School of Resources and Safety Engineering, Chongqing University, Chongqing 400044, China

ARTICLE INFO

ABSTRACT

Knowledge of past hydrological cycling and continental weathering under greenhouse climate conditions helps understand extreme climatic events that are currently occurring. Previous studies of marine strata have reported enhanced hydrological cycling and continental weathering during the Jenkyns Event (JE, also known as the Toarcian Oceanic Anoxic Event; ca. 183 Ma). We undertook a sedimentological and geochemical investigation of semi-deep to deep lacustrine deposits that correspond to the Jenkyns Event (i.e., the Da'anzhai Member in the well LQ104X) in the Sichuan Basin, China. Statistical analysis of sedimentological data demonstrates that the tempestites (bioclastic limestones, discrete shell beds, and shell laminae, lenses, and aggregates in mudstones) and hyperpycnites (sandstones and siltstones with normally and inversely–normally graded beddings) occurred in the Jenkyns Event, which is indicative of enhanced hydrological cycling. Hyperpycnites associated with flooding events developed in the upper part of the Jenkyns Event. Geochemical data suggests an intensified continental weathering during the Jenkyns Event. However, weaker chemical weathering recorded in the upper part of the Jenkyns Event compared with the lower part. The enhanced hydrological cycling increased the transportation during the upper part of the Jenkyns Event, which weakened the chemical weathering in the provenance area and resulted in low CIA (chemical index of alteration). The correlation with sea surface temperatures implies that elevated temperatures during the Jenkyns Event lead to enhanced hydrological cycling, increased frequency of storms and floods, and intensified continental weathering.

1. Introduction

Enhanced hydrological cycling and intensified continental weathering due to global warming result in an increased frequency of extreme climatic events, such as storms, floods, and debris flows (Mitchell, 1989; Stott, 2016). Such weather events modify continental and oceanic ecosystems and affect society. Therefore, studies of hydrological cycling and continental weathering in past greenhouse climate intervals are vital to understanding ongoing extreme climate events. There have been numerous warm intervals in Earth's history, including the Late Permian (Montañez et al., 2007), the Early Jurassic (Han et al., 2018; Hu et al., 2020), and the Paleocene–Eocene thermal maximum (Robert and Kennett, 1994). The Jenkyns Event (JE is also known as the Toarcian Oceanic Anoxic Event (T-OAE); ca. 183 Ma) occurred during Early Jurassic hyperthermal intervals (Jenkyns, 1988; Hesselbo et al., 2000, 2007; Dera et al., 2009, 2011; Müller et al., 2017; Suan et al., 2010). Previous studies have shown that sea surface temperatures increased by 7 °C during the JE, and the hyperthermal conditions lasted for ca. 900 kyr (Suan et al., 2008). Increased sea surface temperatures during the JE caused hurricanes and tropical cyclones (Krencker et al., 2015), and tempestites (Leonowicz, 2011) or turbidites (Hesselbo et al., 2007) were widely developed along continental shelf regions. Studies of marine and marginal-marine deposits also suggest a significant increase in continental weathering intensity during the JE (Hesselbo and Pieńkowski, 2011; Hermoso and Pellenard, 2014; Ruebsam et al., 2020). Enhanced hydrological cycling and intensified continental weathering would have theoretically affected marine, marginal-marine and lacustrine settings (Pieńkowski, 2004; Leonowicz, 2011; Brański, 2012). Therefore,

lacustrine deposits can provide additional records of continental weathering and hydrological cycling variations in greenhouse climate conditions.

The Lower Jurassic lacustrine sedimentary rocks in the Sichuan Basin, particularly the Da'anzhai Member, consist of bivalve-bearing mudstones and shales (Sichuan Geology and Mineral Resources Bureau, 1991). The lake expanded and was larger than 26×10^4 km^2 during the deposition of the Da'anzhai Member. The Re—Os ages (ca. 183 Ma; Xu et al., 2017) and a ~ 4‰ negative organic carbon isotope excursion (CIE) of mudstones in the Da'anzhai Member suggested that these mudstones corresponded to the Jenkyns Event (Liu et al., 2020). Preliminary studies have identified tempestites that were developed in the Da'anzhai Member (Feng et al., 2015). This paper presents an integrated sedimentological and geochemical study of semi-deep to deep
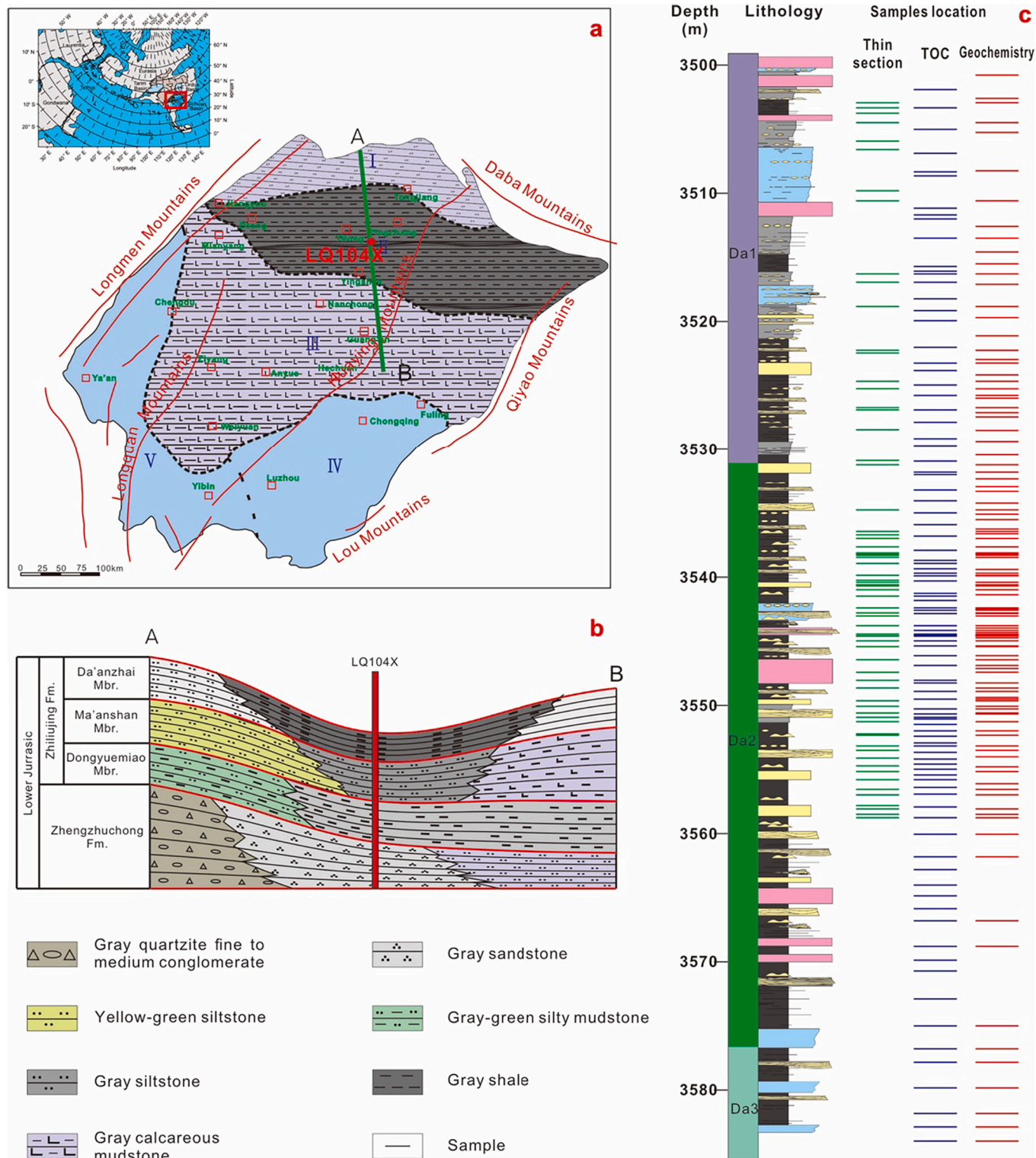

Fig. 1. a) Sketch map showing locations of the Well LQ104X and the Early Jurassic lithofacies and paleogeography in the Sichuan Basin; b) Samples location for TOC, geochemistry analysis, and thin section; c) Transverse profile showing the development of the Lower Jurassic in the Sichuan Basin.

lacustrine facies rocks of the Da'anzhai Member from the well LQ104X in the Sichuan Basin and compares our record of the Jenkyns Event with those from marine sediments.

2. Geological settings

The Sichuan Basin transitioned from a marine platform to a foreland basin in the middle of the Late Triassic Xujiahe Formation (Xia et al., 1982). The Indosinian Orogeny, from the end-Triassic to the Early Jurassic, involved episodic compressional thrusting eastward and southward of Bayan Har Mountains and Qinling orogenic belts in the west and north of the Sichuan Basin. Subsequently, the region tectonic activity tended to be calm, and the Lower Jurassic sediments were deposited. The paleocurrent fall in a range of directions from north to south and from northeast to southwest during the Early Jurassic (Li et al., 2014). In addition to sedimentary rock and granite, there is large volume of mafic rocks, such as gabbro, biotite-hornblende-granite, biotite-bearing granite and plagioclase granite, outcropped in the South Qinling (Sichuan Geology and Mineral Resources Bureau, 1991) in the north of the well LQ104X. Mafic dike swarms are also widely distributed in North Daba Mountain trending in NW-SE direction, intruding the Early Paleozoic strata (Zhou et al., 1999; Zou et al., 2001; Hu et al., 2003).

Due to the warm and humid climate and increased lake level, the lake area expanded during the Early Jurassic to >26 × 10⁴ km². The depositional architecture and facies were distributed in an east-west extension. The sedimentary center of the lake basin was located in Yingshan-Yilong area (Li et al., 2013; Feng et al., 2015; Fig. 1). The Lower Jurassic strata comprise the Zhenzhuchong Formation and the overlying Ziliujing Formation (Chen et al., 2006). The Ziliujing Formation can be subdivided into the Dongyuemiao, Ma'anshan, and Da'anzhai Members from base to top (Sichuan Geology and Mineral Resources Bureau, 1991; see Table 1 for more detailed lithology). After a short interval of lake regression during deposition of the Ma'anshan Member, a lake transgression occurred during deposition of the Da'anzhai Member (Fig. 1). The Da'anzhai Member in the well LQ104X was semi-deep to deep lake facies black mudstones and shales containing abundant late Early Jurassic fossils, such as bivalves of *P. hupehensis*, *Cuneopsis sichuanensis*, and *C. johannisboehmi*, and the ostracods of *Darwinula sarutirmensis* and *Metacypris* sp. Wang et al. (2010) also found diverse freshwater bivalves, ostracods, and conchostracans in the Lower Jurassic deposits in the central region of the Sichuan Basin. A *Re*—Os age for the Da'anzhai

Member from Core A (115 Km west away from the well LQ104X) was 180 ± 3.2 Ma (Xu et al., 2017).

3. Samples and methods

The well LQ104X is located in Dazhou City, Sichuan Province (Fig. 1a). For the sedimentological investigations, the drill core was logged in detail. Seventy-two samples were collected for thin-section observations under an optical microscope (Fig. 1c), and each thin-section was scanned on an Epson Perfection 3170 flatbed scanner.

Clay minerals were identified by XRD on oriented mounts of non-calcareous clay-sized particles at the Wuxi Research Institute of Petroleum Geology, SINOPEC. The clay fraction was separated from the suspension by differential settling according to Stoke's Law. Oriented specimens were prepared by smearing a paste of the <2 μm fraction onto a glass slide (Moore and Reynolds, 1997; Środoń, 2006).

Major element contents were determined by X-ray fluorescence (XRF) spectrometry at ALS Chemex, Guangzhou, China, with an analytical uncertainty of ±5%. Trace element abundances were determined by inductively coupled plasma–mass spectrometry (ICP–MS) at ALS Chemex, Guangzhou. The analytical uncertainty is better than ±10% for most analyzed elements. TOC contents were determined with a Leco CS-200C–S analyzer at ALS Chemex, Guangzhou. TOC content was also calculated based on ΔlgR (TOC = ΔlgR×10$^{2.297-0.168\ 8LOM}$; ΔlgR is the curve separation measured in resistivity cycles; LOM is level of organic maturity) according to Passey et al. (1990).

The major and trace element compositions of the analyzed samples were discussed with reference to the estimated average concentrations of elements in the upper continental crust (UCC; Taylor and McLennan, 1985; Hu and Gao, 2008) and upper crust of the South Qinling (SQ; Gao et al., 1998). To constrain the degree of continental weathering, we used several geochemical indices, including the chemical index of alteration (CIA; Nesbitt and Young, 1982), and its modified forms CIW (Harnois, 1988), PIA (Fedo et al., 1995), CPA (Buggle et al., 2011), CIX (Garzanti et al., 2014a, 2014b), and WIP (Parker, 1970). Weathering intensities were also calculated from mobile elements by comparing the concentration of each mobile element relative to that of immobile element Al (e.g., α_{Ca}^{Al} = [Al/Ca]$_{sediment}$/ [Al/Ca]$_{source\ rock}$; Gao et al., 1998; Gaillardet et al., 1999; Garzanti et al., 2013a, 2013b). REE data were normalized to their concentrations in CI carbonaceous chondrites (McDonough and Sun, 1995).

Table 1
Lithology, lake level, and tectonic activity of the Sichuan Basin in the Lower Jurassic.

Strata			Lithology			Lake level	Tectonic activity
	Formation	Member	Northern Sichuan Basin	Northeast of the Sichuan Basin (in the study area)	Central–southern Sichuan Basin		
Lower Jurassic	Ziliujing Formation	Da'anzhai Member	Siltstones interbedded with mudstones	Blackish gray and black shales containing abundant bivalves of *P. hupehensis*, *Cuneopsis sichuanensis*, and *C. johannisboehmi*, and the ostracods *Darwinula sarutirmensis* and *Metacypris sp*	Grayish calcareous mudstones	Rise	Calm
		Ma'anshan Member	Alternated yellow–green and gray–green siltstones and mudstones	Blackish shales interbedded with siltstones	Purplish red calcareous mudstones	Fall	Calm
		Dongyuemiao Member	Gray–green and red argillaceous siltstones	Blackish gray calcareous siltstones and shales, which are rich in the bivalves *Pseudocardinia carinata*, *P. elliptica*, and *P. minuta*	Blackish gray and black siltstones and shales interbedded shell-bed, which are rich in the bivalves P. kweichouensis, *P. hupehensis*, *P. minuta*, *P. carinata*, *P. elliptica*, P. submagna	Rise	Calm
	Zhenzhuchong Formation		Fine- to medium-grained sandy conglomerates and quartzose sandstones	Purple–red to gray–green siltstones	Silty mudstones	Rise	Calm

Table 2

Taphonomic characteristics of shells and sedimentary structures of seven event beds.

Facies		Taphonomic characteristics of shells	Sedimentary structures	Interpretation
Limestone	Bioclastic limestone	1. The shell fragments consist of conchostracans and bivalve hinges and are parallel to the bedding. 2.The shells are the most broken and rounded, with lengths of ~0.2 mm and thicknesses of ~0.4 mm. 3. The double-layer structure of the shells has been destroyed by boring and later recrystallization.	1. Erosional base. 2. 3D HCS, a length of ~60 cm and a height of ~20 cm characterized by third-order lamina truncating second-order boundaries.	**High-energy storm currents (proximal tempestites)** 1. Shell abrade against each other in storm currents resulting in broken and rounded fragments. 2. Reworking and re-exposion of the shells by storm currents allow micro-organisms to attach on shells in favor of boring. 3. Tractive currents of storm during the waxing stage erode previous sediments and form an irregular erosional base. 4. HCS is formed in high-intensity oscillatory flows or oscillatory-dominated combined-flows with high aggradation rates
Mudstone	Discrete shell bed	1. The shells aligned parallel to the bedding. 2. Most of the shells are moderately sorted and have sharp edges, with lengths of >2 mm and thicknesses of ~0.2 mm. 3. Most of the shells maintain the double-layer structure.	1. Erosional base overlain by graded bedding which is manifested by decrease of shell size upward.	**Storm currents (tempestites)** 1. Shells were winnowed from proximal localities and entrained in a high viscosity flow induced by storm current. 2. High viscosity flow prevents shells from abrasion and organism boring. Thus, the original double-layer internal structure and sharp edges of the shells were preserved. 3. the erosional base formed during the waxing stage of storms, the shells and matrixes suspended by storm currents would settle down in waning stage to form a normally graded bedding seated on erosional base.
	Shell laminae	1.The shells are concave or convex upwards along wave ripples. 2. The shells in the laminae are all bivalves, whereas ostracods occur mainly in the matrix. 3. The shells are small, well sorted, and most of the shells maintain the double-layer structure.	1. Wave ripple	**Storm currents (distal tempestites)** 1. These relatively small and thin allochthonous bivalves were transported to deep-water deposition by storms from nearshore areas. 2. Wave ripples are formed in wave flow caused by storms.
	Shell lens and aggregate	1. Orientation of shell is random. 2. Bad sorted. Intact large bivalve shells (8–10 mm) and small shell fragments (~0.5 mm) with sharp edged occur in both the lenses and aggregates. 3. Original double-layer structures are perfectly preserved.	1. Massive bedding	**Hurricanes** 1. The high viscosity and particle concentration flows caused by hurricanes can eliminate maximumly the abrasion of the entrained shells and reduce the opportunity for boring. 2. The High viscous flow quickly cease, leading to chaotic orientations of the shells and bad sorted.
	Shelly mudstone	Few shells	1. Small-scale HCS 2. Erosional base 3. Homogeneous mudstone. 4. Banded clay layers.	**Storm currents (tempestites)** 1. HCS and erosional base are formed in storm currents. 2. Homogeneous and banded mudstones might be fluidized mud flow sediments that were deposited in currents with a high sediment concentration.
	Shelly siltstone	Few shells	*Shelly siltstones associated with storm* 1. Fine silt lenticels with offshoots. 2. Wave ripples with rounded and symmetrical ridges. 3. Mottled siltstone. 4. Draped muds in the crest of the wave ripples.	**Strom currents (tempestites)** 1. Offshoots in fine silt lenticels and wave ripples with rounded and symmetrical ridges suggest storm current and high energy. 2. Mottled and draped muds are mud flow sediments that were deposited in currents with a high sediment concentration
			Shelly siltstones associated with floods 1. Normally graded bedding with erosional base. 2. Inversely-normally graded bedding with gradually transition in the middle part. 3. Plenty of plant debris	**Floods (distal hyperpycnites)** 1. These two types of graded beddings might both be related to hyperpycnal currents caused by flood events. 2. Gradually transition in the middle part of the inversely-normally graded bedding indicated that the flow energy of flood peak is not enough to erode previous sediments. 3. Plant debris might be transported by floods.
Sandstone	Sandstone	No shell	1. Normally graded bedding with erosional base. 2. Inversely-normally graded bedding with an erosional surface. 3. More high plant debris than that in shelly siltstones.	**Floods (Proximal hyperpycnites)** An erosional surface in the middle part of the inversely-normally graded bedding indicated that the flow energy of flood peak is enough and the flood peak persists for a long time, and previously deposited inversely graded bed is partly denuded.

4. Results

4.1. Lithology

The Da'anzhai Member in the well LQ104X contains three major lithofacies: limestone, mudstone, and sandstone. Mudstones account for 95%, and sandstones and limestones account for 5%. A total of seven sub-facies associated with storm and flood events are summarized in Table 2. According to the background deposition of these sub-facies, the sediment transport and depositional processes, as well as the hydrological conditions which are inferred by taphonomic characteristics of shells and sedimentary structures of event beds (Davies et al., 1989), the proximal and distal event beds and their variabilities are outlined below. The proximal event beds are generally deposited in background sediments dominated by coarse-grained deposits. In contrast, the distal event beds are developed in background deposits characterized by fine-grained deposits, such as mudstones with horizontal bedding.

4.1.1. Proximal

Proximal event beds, including proximal hyperpycnites and tempestites represented by sandstones and bioclastic limestones, are generally thick-bedded, more than one meter (Fig. 2a, b) and mainly occurred in siltstone and sandstone background lithofacies (Fig. 1). Sandstones, proximal hyperpycnites, are distributed in 3507 to 3523 m and 3570 to 3577 m and develop in association with bioclastic limestones and discrete shell beds (Fig. 1). Most sandstones have inversely–normally graded bedding with an erosional surface in the middle part (Fig. 2a). Bioclastic limestones are more common than sandstones, distributed in intervals from 3500 m to 3507 m, from 3545 m to 3548 m, and from 3565 m to 3571 m (Fig. 1). The content of shells is >85%, and shells in most bioclastic limestones are densely packed (Fig. 3a). Sands and crystalized calcite can be seen in the less densely packed area in bioclastic limestones (Fig. 2a, b).

4.1.2. Intermediate

In the intermediate event beds, tempestite and hyperpycnites, are predominantly thin to medium-bedded (0.1 to 1 m), including discrete shell beds in mudstones, shelly mudstones, and shelly siltstones (Fig. 2c, e, f).

Discrete shell beds mainly occur in intervals from 3536 m to 3539 m and 3558 m to 3559 m (Fig. 1). The event beds are interbedded in mudstones with wavy or massive bedding (Fig. 2a, f). They are usually combined with shelly mudstones and shelly siltstones (Fig. 1). The shells at the bottom are densely packed, while those are dispersed, and the residual fine-grained sand matrix is found in the upper part of the discrete shell bed (Fig. 3c, d).

Homogenous shelly mudstones (Fig. 4a) and shelly siltstones with offshoots and wave ripples (containing internal foreset laminae) both contain few shells (Fig. 4b, c) and are interbedded in the massive fine-siltstone (Fig. 1). Shelly mudstones mainly occur in 3532 m to 3540 m, whereas shelly siltstone is the most common sub-facies, which is distributed in intervals from 3528 m to 3532 m and from 3513 m to 3521 m. Shelly mudstones always occur in the form of banded clay layers (Fig. 4d) and draped mud (Fig. 4e, f) in combination with shelly siltstones (Fig. 1).

4.1.3. Distal

The distal tempestite event beds are very thin to thin-bedded (0.03 to 0.1 m), including shell laminae, shell lenses, and aggregates (Fig. 2g, h).

Shell laminae are distributed between 3535 m and 3541 m (Fig. 1). The shells occur as laminae intercalated in mudstones with wavy bedding (Fig. 3e). This sub-facies occurs in combination with shell lenses and aggregates and shelly siltstone (Fig. 1). The shell in this event bed is moderately densely packed, in which the matrix is fine silt and mud (Fig. 3e).

Shell lenses and aggregates mainly occur between 3534 m to 3541 m (Fig. 1). This sub-facies is characterized by shells gathering into lenses and aggregates in massive mudstones (Fig. 3f). The matrix in this event bed is mud, which is the same as the surrounding rocks (Fig. 3f).

4.2. Clay minerals

The clay fraction from the well LQ104X is dominated by illite (24–58%, with an average of 39%) and followed by illite-smectite mixed-layers (9–60%, with an average of 35%) and chlorite (5–30%, with an average of 15%). The kaolinite is slightly low (3–20%, with an average of 10%). Kaolinite/illite (0.06–0.42, average of 0.21) and kaolinite/ (illite + chlorite) ratios (0.05–0.29, average of 0.16) reflect the varied clay mineral composition. The kaolinite/ (illite + chlorite) ratio has a high average value of 0.17 from 3555 to 3535 m, a low average value of 0.1 from 3535 to 3517 m, and then recovers 0.16 from 3517 to 3500 m.

4.3. Geochemistry

Geochemical data for 122 fresh samples are listed in Supplementary Tables 1–4. The range of variation in the element concentrations is wide (SF. 1a). The samples can be divided into three groups based on UCC-normalized Ca and Ti values (Ca_N and Ti_N). Group I have $Ca_N < 1$ and $Ti_N > 1$, and include most of the analyzed samples. The normalized values of the alkaline earth metals (Ca_N and Sr_N) are much <1 (SF. 1b). Group II samples have $Ca_N > 1$ and $Ti_N > 1$. The compositions of group II samples are generally similar to those of group I, but the former has higher Sr contents, with some samples having $Sr_N > 1$ (SF. 1c). Group III samples have high Ca_N values and low Ti_N values. The compositions of group III samples are different from those of group I and II samples. Apart from Ca and Sr, UCC-normalized element concentrations of group III samples are all <1 (SF. 1d).

All the samples have chondrite-normalized REE patterns characterized by light REEs enrichment, heavy REEs depletion, and negative Eu anomalies (SF. 2a). The REE patterns of group I and II samples are similar, and are comparable to those of the upper continental crust of the SQ (SF. 2b). However, group III samples have lower total REE contents and more significant depletion of heavy REEs (SF. 2c).

Chemical weathering and paleoclimate indices are calculated and listed in Tables 3 and 4. The correlation coefficients between the CIA and CIW, PIA, CPA, and CIX are >0.90, and the correlation coefficient between the CIA and α_E^{Al} is >0.75 (SF. 3).

5. Discussion

5.1. Sedimentological evidence for storms, hurricanes, and flood events

5.1.1. Shell enrichment and mud as indicators of storm and hurricane events

The four shell-rich lithofacies (i.e., bioclastic limestone, shell beds, shell laminae, and shell lenses and aggregates) in the well LQ104X were formed associated with storm or hurricane events. The ubiquitous erosional base (Fig. 3d) and HCS in bioclastic limestones were observed in the well LQ104X and an outcrop section 138 km away. HCS is a typical sedimentary structure indicating the storm action (Dott Jr and Bourgeois, 1982; Duke, 1985; Cheel et al., 1993). High-energy storm flows with strong shear force often form an irregular erosional base (Kreisa, 1981; Gao et al., 1999), and also selectively winnow relatively fine particles and cause shell accumulations (Kidwell, 1986, Kidwell and Holland, 1991; Fick et al., 2018). When the storm energy and winnowing are weak, residual sandy matrix remains between shells (Fig. 3a); while the energy is intense, the sandy matrix can be removed, leaving cavities between the shells that later become filled by calcite (Fig. 3b). In addition, the broken and rounded shells with boring and later recrystallization also suggest that the bioclastic limestones are tempestites. Storm currents can rework and re-expose the shells and
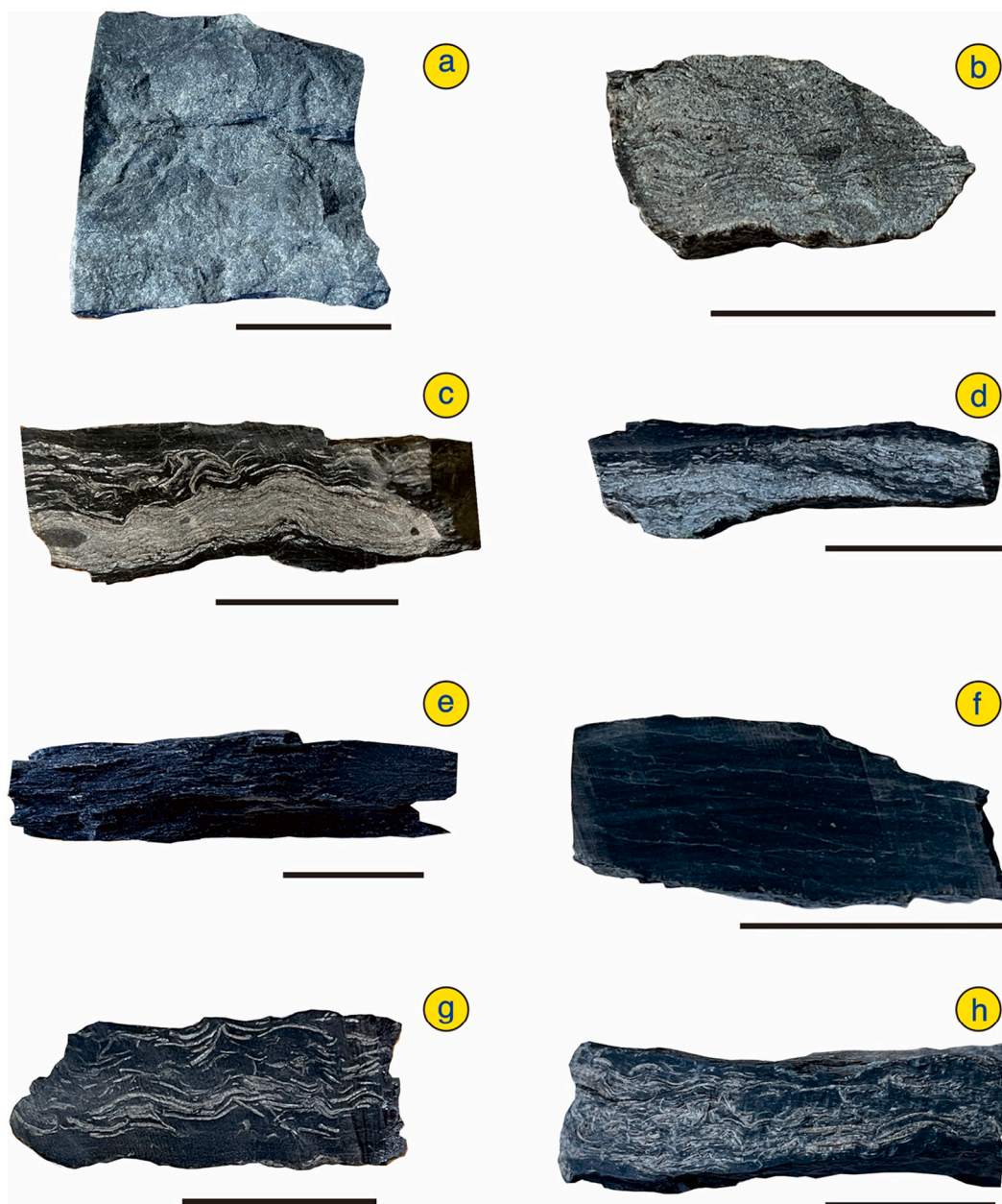
Fig. 2. Major lithofacies of the Da'anzhai Member in the Well LQ104X. a) Sandstone; b) Bioclastic limestone; c) A discrete shell bed in mudstone; d) Shell-bedded mudstone; e) Shelly mudstone; f) Shelly siltstones; g) Shell-laminar mudstone; h) Shell-aggregation mudstone. Scale bar = 2 cm.

allow microorganisms to adhere to the surface of shells resulting in the boring (Chamberlain and Westermann, 1976).

In the discrete shell beds lithofacies, erosional bases are overlain by normally graded beddings related to high-energy storm currents are ubiquitous (Fig. 3c, d; Wang and Horwitz, 2007). In the waxing stage of storms, the high energy currents erode and winnow sediments, resulting in an erosional base (Fig. 3c). In the winnowing stage, the suspended shells would settle down, forming a normally graded bedding (Figs. 3c). The well-preserved double-layer structure and thinner nature of the shells suggested these shells were winnowed from proximal localities and entrained in a flow with a high particle concentration and viscosity during storms. High particle concentration and viscosity hampered the abrasion and boring of shells, and thus the original double-layer internal structure and sharp edges of the shells were preserved. Reports of discrete shell beds formed by storms are common (Davies et al., 1989; Dattilo et al., 2012; Puga-Bernabéu and Aguirre, 2017).

The concave and convex shells within the shell laminae in mudstone lithofacies are arranged in harmony with wave troughs and crests, respectively, suggesting that waves reworked these shells as they settled (Fig. 3e). The shells in the laminae are all bivalves, whereas ostracods occur mainly in the matrix, which is suggestive of deep-water deposition. These allochthonous bivalves were transported by offshore-directed currents and oscillatory flow generated by storms from near-shore areas.

Both fragmented and intact shells with chaotic orientation occur in the lenses and aggregates, which have experienced minor subsequent diagenetic alteration (Fig. 3f). We speculate that these lithofacies may be related to high-viscosity flows caused by hurricanes. The high-viscosity flows quickly cease and lead to chaotic orientations of the shells (Puga-Bernabéu and Aguirre, 2017). The mudstones and siltstones with shell lenses and aggregates have homogeneous and massive bedding, which is consistent with deposition from sediment-rich and highly viscous flows.

Fig. 3. Shell taphonomy characteristics of the Da'anzhai Member in the Well LQ104X. a) Micrograph of bioclastic limestone with silty and sandy matrix (3504.50 m); b) Close-up micrograph showing calcites in pores in bioclastic limestone (3542.46 m); c) Thin section scanning showing a shell bed changes gradually to mudstone (3530.95 m). In the upper part of the photo, the erosional base is overlaid by normally graded beddings, which is a typical sedimentary structure of storm deposition; d) Thin section scanning showing a discrete shell bed 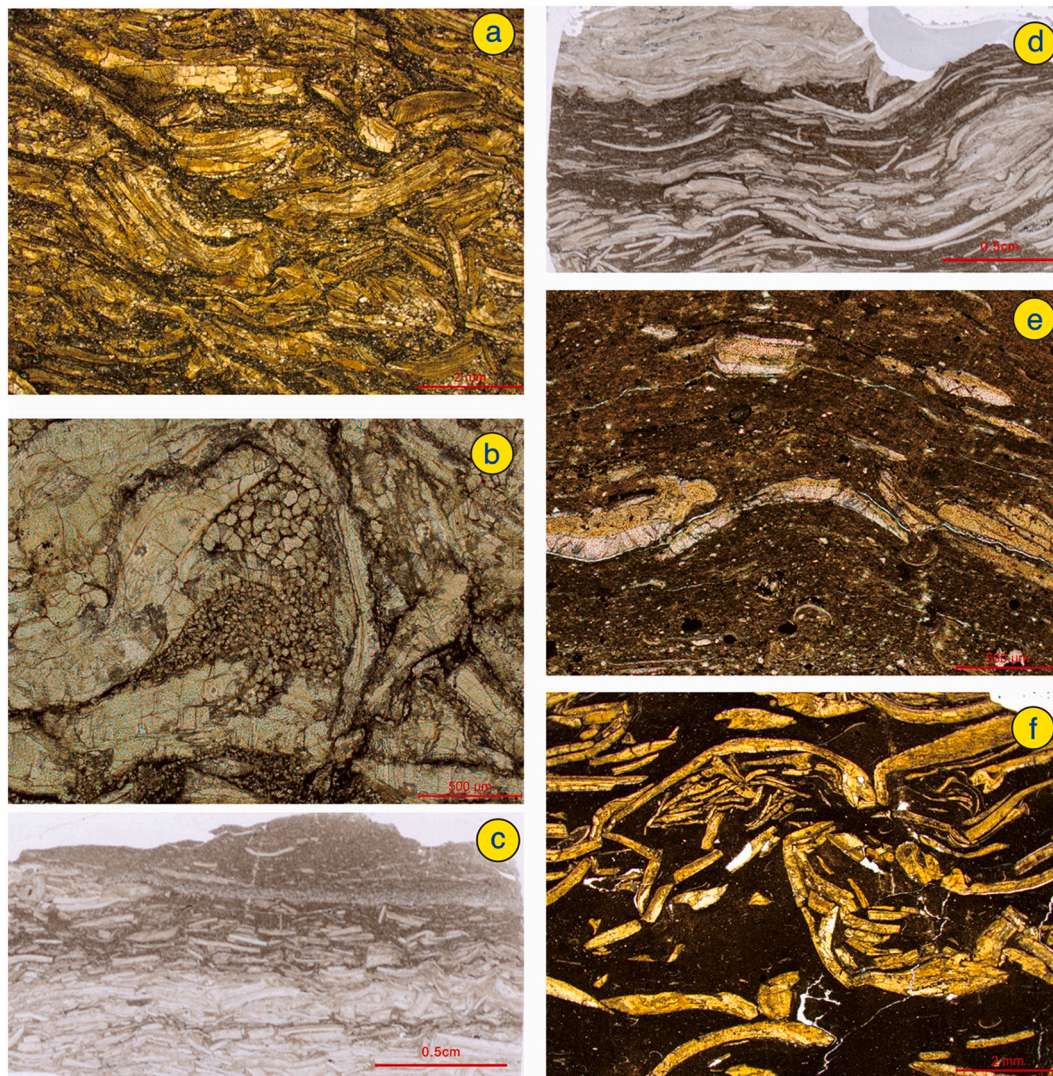in the lower part of the photo and a bioclastic limestone with an erosional base indicating high-energy flows in the upper part of the photo (3526.76 m); e) Micrograph showing a shell laminar with wave ripples (3544.50 m). Siltstone with a normally graded bedding can be recognized in the lower part of the photo; f). Micrograph showing the internal structure of a shell aggregation, in which intact tests and fragments of bivalves are mixed together, and most of the tests have original double layers, i.e., the columnar outer layer and the laminated inner layer (3537.70 m);

Apart from the shell-rich lithofacies, the siltstones and clayey mudstones also represent tempestite deposits (Fig. 1). In outcrops, small-scale HCS is developed in the siltstones and silty mudstones (Fig. 4g). On a microscopic scale, fine silt lenses with offshoots (Fig. 4b), wave ripples with round and symmetrical ridges (Fig. 4c), and mud drapes (Fig. 4f) are common. The sedimentary structures described above are related to storm events (Jennette and Pryor, 1993). There are also many layers of homogeneous mudstones (Fig. 4d) and mottled claystone to siltstone (Fig. 4e), and mudstones with thickness of 0.5–10 mm that have a sharp or erosional basal surface (Fig. 4h, i). These might be fluidized mud flow sediments associated with strong and steady storm wave-generated flows or flood events (Faas, 1991; Nishida et al., 2013; Hill et al., 2007).

5.1.2. Graded bedding as an indicator of flooding events
Graded bedding is an essential indicator of flooding events (Mulder et al., 2001, 2003). Normally and inversely–normally graded beddings are common in the sandstones and siltstones (Figs. 2a and 4j). These two types of graded beddings might both be related to hyperpycnal currents caused by flood events (Mulder and Chapron, 2011). Due to high sediment concentration and density, hyperpycnal currents erode the underlying sediment as it moves forward. When a flood is in the waxing stage of discharge, the energy of the hyperpycnal current gradually increases and forms a bed with inverse grading. In the waning stage, a bed with normal grading is deposited. The grain size reaches a maximum at the transformation between the inversely and normally graded bedding, representing the peak of the flood energy. Thus, a coupled inversely–normally graded bedding develops from a hyperpycnal current (Mulder et al., 2001).

If the flood peak persists for a long time, the hyperpycnal current will partly or entirely denude the previously deposited inversely graded bedding and form an erosional surface. However, the presence of just a normally graded bedding cannot be directly interpreted as the inversely graded bedding has been completely denuded. It is also possible that the flood discharge did not reach the threshold for forming a hyperpycnal current. In this case, the flow may develop involving hypopycnal,
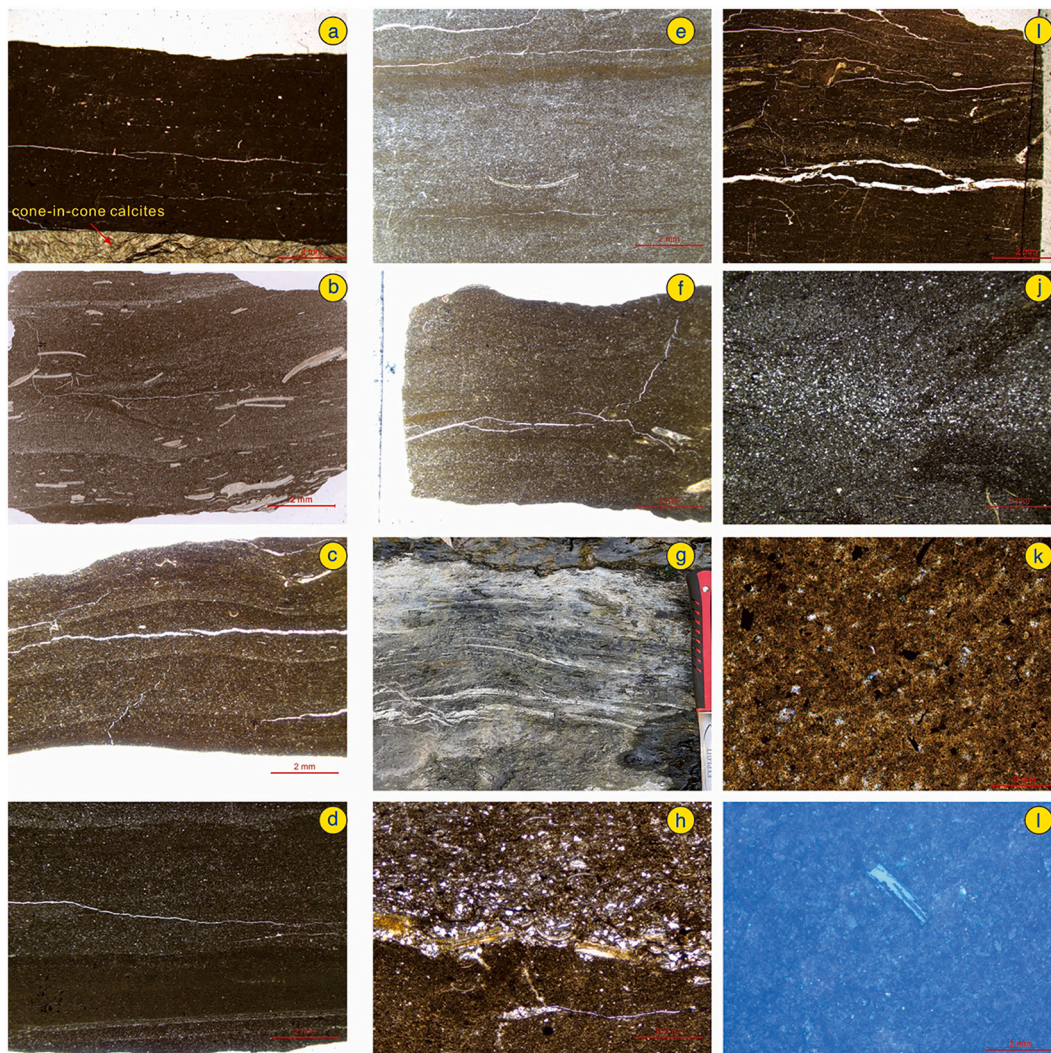
Fig. 4. Typical sedimentary structures of the Da'anzhai Member in the Well LQ104X. a) Micrograph showing a diagenetic contraction filled by calcites in a homogeneous clay mudstone (3540.45 m); b) Thin section scanning showing fine silt lenticels with offshoots (3525.28 m); c) Thin section scanning showing four sets of wave ripples with rounded and symmetrical ridges (3539.90 m); d) Micrograph showing homogeneous and banded clay layers is underlain by siltstones with an erosional base (3554.10 m); e) Micrograph showing mottled siltstones with draped muds (3553.25 m); f). Thin section scanning showing draped mud in the crest of the wave ripples within siltstone (3543.10 m); g) A small HCS in siltstones in an outcrop section 138 km away from the Well LQ104X; h) Micrograph showing normally graded bedding can be seen above the erosional base (3557.05 m); i). Thin section scanning showing a normally graded bedding with an erosional base in the shelly mudstone (3544.50 m); j) Micrograph showing an inversely-normally graded bedding in shelly siltstone (3551.36 m); k) Micrograph showing abundant terrigenous detritus and plants occur in the upper of inversely-normally graded bedding (3530.20 m); l). Reflected light petrography of terrigenous plants.

homopycnal, or mesopycnal currents. The suspended terrigenous detritus that was transported by these currents would settle and develop a normally graded bedding with a sharp base. In this study, most of the normally graded beddings have an erosional base, which may have formed from hyperpycnal currents triggered by floods.

As described above, a normally graded bedding with an erosional base can also form during the waning stage of a storm event. The nature of the grains in such beds can be used to distinguish storm and flood deposits. Floods transport more terrigenous detritus into a basin, including more fragments of higher plants. However, tempestites contain mainly reworked detritus from a basin, such as shells. Therefore, siltstones with normal graded bedding above an erosional base shown in Fig. 4h with more shells are inferred to have been related to storm events. In contrast, siltstones shown in Fig. 4k, with the higher plant fragments but few shells, are inferred to have been related to flood events.

5.1.3. Deposition of tempestites and hyperpycnites

Based on sedimentological interpretation and statistical data of sedimentary characteristics, we found that storms, hurricanes, and floods were frequent but uneven during the Jenkyns Event, and the energy of storms and floods changed significantly (Fig. 5).

Generally, proximal tempestites occur mainly at depths of 3500–3517.9 m, 3546.1–3548.4 m, and 3564.3–3570 m. In addition, there are also two intervals with typical distal tempestites: 1) Depths of 3548.4–3560.0 m, the Pl-To CINE (Pliensbachian-Toarcian boundary). The lower part of this interval is dominated by shell laminae and discrete shell beds interbedded with mudstones that have erosional bases and wave ripples. In contrast, the upper part is mainly shelly siltstones with wave ripples. It shows that the storm energy weakened upward. 2) Depths of 3517.5–3546.1 m corresponding to the Jenkyns Event (the main stage of NCIE, Liu et al., 2020). Distal tempestites are primarily represented by shelly siltstones, shell laminae, and discrete shell beds. Tempestites gradually decrease upwards in this interval. Shell lenses and aggregates within mudstones caused by hurricanes can only be observed

Table 3

Weathering indices of 122 samples from 3490 m to 3585 m in the well LQ104X in the Sichuan Basin.

Depth(m)	CIA	CIW	PIA	CIX	CPA	WIP	α_{Ca}^{Al}	α_{Mg}^{Al}	α_{Na}^{Al}	α_{K}^{Al}	α_{Rb}^{Al}	α_{Sr}^{Al}	α_{Ba}^{Al}
3490.20	73.44	82.88	80.36	79.47	90.64	35.34	3.34	2.63	3.41	1.18	0.77	1.84	1.59
3491.90	75.96	86.61	84.42	80.70	92.82	40.94	4.47	3.37	4.58	1.18	0.75	1.80	1.52
3494.00	85.14	100.00	100.00	85.14	100.00	3.29	–	1.87	4.83	1.16	0.75	0.04	0.60
3496.60	68.00	77.73	74.01	75.34	87.47	41.13	2.41	2.78	2.83	1.15	0.80	0.97	1.51
3498.81	72.26	81.42	78.72	77.30	87.88	42.58	3.82	2.32	2.54	1.26	0.94	2.28	1.55
3499.60	75.59	88.69	86.32	79.41	94.01	44.06	5.42	3.01	7.82	1.34	0.82	0.68	1.52
3500.78	74.22	84.54	82.04	79.62	91.62	37.85	3.78	2.05	4.20	1.17	0.82	1.31	1.48
3502.60	72.84	84.69	81.71	77.97	91.71	42.62	3.82	2.30	3.84	0.97	0.64	2.14	1.27
3502.95	73.46	85.65	82.80	78.28	92.27	44.00	4.12	2.72	4.18	1.04	0.68	1.75	1.36
3504.50	75.66	86.99	84.70	80.19	93.04	4.54	6.01	0.59	6.69	1.47	0.82	0.08	0.58
3505.25	71.53	83.64	80.31	76.90	91.09	47.08	3.53	2.42	3.82	0.93	0.61	2.42	1.28
3508.25	71.68	81.75	78.77	77.92	89.96	35.50	3.57	2.33	3.57	1.31	0.79	2.63	1.46
3510.60	66.72	72.46	69.87	76.40	84.03	28.19	1.82	2.03	1.84	1.64	1.30	1.95	2.11
3512.60	76.94	89.83	87.78	78.97	92.61	43.95	10.33	2.13	4.89	0.95	0.59	2.42	1.06
3513.52	76.26	89.02	86.81	79.34	93.26	44.73	6.76	2.11	5.02	1.01	0.65	2.61	1.33
3514.59	76.83	89.62	87.55	79.46	93.21	44.94	8.02	2.36	4.99	1.05	0.69	2.33	1.40
3515.52	75.56	88.79	86.41	79.34	94.06	45.92	5.47	2.37	5.93	0.96	0.59	2.48	1.22
3516.30	75.07	85.34	83.02	78.04	89.21	44.14	6.81	2.34	3.04	1.24	0.83	2.59	1.49
3517.12	68.46	75.46	72.66	77.03	86.01	37.50	2.48	1.99	2.48	1.68	1.08	2.75	1.79
3518.85	78.37	87.80	86.13	82.88	93.50	10.87	4.97	2.08	9.01	2.88	2.11	0.11	1.01
3519.72	66.14	72.19	69.39	75.79	83.85	28.81	3.15	2.21	6.00	2.70	0.60	2.18	1.26
3521.15	75.77	89.30	86.98	79.37	94.35	42.59	6.34	2.12	5.85	0.94	0.60	2.89	1.27
3522.27	67.50	75.80	72.40	75.65	86.23	43.47	2.16	2.34	2.38	1.17	0.76	1.50	1.43
3523.00	76.00	90.75	88.53	79.06	95.15	42.13	6.78	2.32	6.74	0.88	0.54	1.44	1.16
3523.29	71.38	81.72	78.63	77.57	89.94	30.69	3.49	0.88	3.49	1.24	0.66	1.13	1.17
3524.20	76.52	89.64	87.50	80.06	94.54	43.71	5.97	2.43	6.11	0.97	0.58	2.35	1.21
3524.70	76.41	90.75	88.61	79.50	95.15	46.38	6.77	2.10	7.12	0.96	0.58	2.41	1.28
3525.28	69.14	78.34	75.01	76.45	87.85	34.74	2.50	1.21	2.49	1.10	0.75	0.69	1.30
3525.80	75.95	89.85	87.57	79.36	94.65	42.32	6.11	2.33	5.49	0.86	0.55	2.34	1.17
3526.01	76.50	90.72	88.60	79.55	95.04	48.14	6.89	2.64	7.15	0.98	0.59	2.46	1.32
3526.76	74.79	85.50	83.07	79.86	92.18	15.76	7.21	0.67	7.21	2.06	0.77	0.51	1.18
3527.15	76.98	91.01	89.01	80.02	95.29	46.07	6.99	2.77	7.48	1.00	0.62	1.60	1.34
3527.50	76.24	88.20	86.01	80.34	93.73	38.53	5.16	2.52	5.20	1.07	0.65	1.79	1.29
3528.55	71.51	81.88	78.81	77.65	90.04	41.34	3.12	1.81	3.20	1.10	0.71	1.36	1.19
3529.40	76.48	90.42	88.29	79.70	94.97	46.28	6.52	2.73	7.09	1.01	0.65	2.10	1.38
3530.50	75.66	88.32	85.97	79.64	93.80	44.27	5.22	2.68	5.66	1.06	0.65	2.14	1.18
3531.28	73.46	84.78	82.01	78.65	91.76	28.19	3.85	2.26	3.88	1.03	0.65	0.96	1.28
3531.85	77.97	89.74	87.92	79.63	91.95	40.96	12.93	2.17	4.32	1.06	0.66	2.20	1.35
3532.38	77.07	89.35	87.33	79.73	92.95	42.97	7.96	2.39	4.92	1.10	0.67	2.28	1.40
3532.98	74.94	87.45	84.93	79.06	93.11	44.61	4.97	2.42	4.72	0.98	0.61	2.57	1.27
3533.35	76.09	90.32	88.10	78.85	94.24	47.79	7.51	2.74	6.12	0.98	0.58	2.33	1.26
3534.27	77.34	88.21	86.28	80.78	92.72	41.20	6.27	1.81	4.33	1.35	0.92	2.14	1.77
3534.80	75.63	88.84	86.48	79.41	94.09	46.35	5.49	2.58	6.03	1.01	0.60	2.39	1.33
3535.15	75.75	89.38	87.05	79.32	94.39	47.09	5.81	2.60	6.25	0.97	0.58	3.22	1.30
3535.56	77.83	92.29	90.53	79.36	94.45	47.08	13.94	2.73	6.29	0.97	0.57	2.75	1.15
3536.30	75.90	89.19	86.89	79.57	94.28	45.45	5.69	2.61	5.90	0.98	0.58	2.72	1.31
3536.48	76.17	89.23	87.01	79.84	94.31	38.68	5.72	2.90	6.69	1.15	0.71	0.91	1.39
3536.68	78.92	92.72	91.18	81.44	96.22	38.88	8.80	2.82	8.57	0.92	0.53	2.42	1.22
3537.05	73.62	84.70	81.99	78.86	91.71	40.36	3.82	2.65	3.85	1.17	0.71	2.34	1.50
3537.70	76.96	89.44	87.40	80.63	94.43	27.43	7.07	2.32	7.07	1.30	0.62	1.09	1.27
3538.18	77.56	90.80	88.90	80.74	95.18	43.61	6.81	2.74	7.58	1.11	0.62	2.06	1.38
3538.25	75.31	86.72	84.35	79.92	92.89	30.34	5.04	2.65	5.04	1.24	0.66	1.08	1.26
3538.35	78.76	92.18	90.57	80.80	94.99	45.51	10.77	2.84	7.23	1.07	0.61	3.15	1.44
3538.79	78.79	92.63	91.06	80.54	95.06	46.05	12.49	2.84	7.24	1.02	0.58	2.78	1.31
3539.45	77.36	90.37	88.43	80.69	94.94	46.10	6.48	2.85	6.97	0.99	0.59	2.77	1.26
3539.75	78.07	89.63	87.83	81.77	94.53	40.46	5.97	3.18	6.47	1.14	0.65	2.51	1.39
3539.90	78.09	90.77	88.98	80.67	94.28	42.49	8.44	2.84	6.08	1.10	0.63	2.44	1.32
3539.95	78.11	91.53	89.78	81.03	95.58	38.55	7.47	2.94	7.78	1.08	0.62	1.71	1.38
3540.45	78.35	92.25	90.58	81.02	95.97	22.58	8.22	2.71	7.49	1.14	0.66	0.92	1.32
3540.64	73.94	84.03	81.51	79.52	91.32	37.83	3.63	2.36	3.46	1.10	0.66	2.07	1.33
3540.75	77.46	90.33	88.40	80.81	94.92	38.39	6.45	2.83	6.72	1.08	0.65	1.01	1.34
3541.05	77.04	89.75	87.73	80.54	94.54	43.96	6.13	2.68	6.02	1.07	0.64	2.32	1.30
3541.44	78.17	91.13	89.36	81.26	95.36	43.02	7.09	2.88	7.09	1.08	0.62	2.67	1.29
3542.46	87.68	100.00	100.00	87.68	100.00	2.53	–	1.68	7.99	2.30	1.46	0.03	0.30
3542.52	88.24	100.00	100.00	88.24	100.00	2.89	–	1.60	7.59	1.39	0.96	0.03	0.41
3542.60	75.62	85.94	83.72	80.61	92.44	40.12	4.22	2.98	4.35	1.20	0.75	2.13	1.53
3542.65	78.01	89.08	87.27	81.34	93.44	40.97	6.58	3.22	5.16	1.22	0.75	2.57	1.54
3542.85	75.33	85.40	83.15	80.51	92.13	37.54	4.04	2.84	3.71	1.18	0.75	2.59	1.41
3542.90	77.26	88.22	86.27	81.46	93.74	38.50	5.17	3.35	5.31	1.21	0.75	1.64	1.52
3543.10	72.04	82.42	79.46	78.04	90.36	41.65	3.98	2.99	4.66	1.37	0.69	2.70	1.41
3543.86	75.48	85.25	83.05	77.69	88.08	41.23	9.14	2.42	2.58	1.22	0.86	1.24	1.27
3544.05	79.82	92.82	91.43	82.36	96.28	41.94	8.93	3.29	9.57	1.11	0.61	2.56	1.47
3544.21	79.56	92.65	91.21	82.15	96.19	38.43	8.71	3.23	9.12	1.11	0.58	1.96	1.34
3544.38	79.53	92.70	91.26	82.10	96.21	42.11	8.77	3.18	9.40	1.10	0.60	2.73	1.44

Table 3 (*continued*)

Depth(m)	CIA	CIW	PIA	CIX	CPA	WIP	α_{Ca}^{Al}	α_{Mg}^{Al}	α_{Na}^{Al}	α_{K}^{Al}	α_{Rb}^{Al}	α_{Sr}^{Al}	α_{Ba}^{Al}
3544.50	80.03	93.24	91.90	82.42	96.50	37.01	9.52	2.85	8.44	0.97	0.51	2.36	1.17
3544.53	79.16	91.88	90.32	82.02	95.77	41.10	7.81	3.16	8.47	1.11	0.60	2.47	1.40
3544.60	79.31	92.50	91.01	81.94	96.11	43.53	8.52	3.26	8.91	1.10	0.60	2.73	1.37
3544.65	78.91	92.18	90.60	81.64	95.93	38.58	8.14	3.08	7.74	1.07	0.59	1.94	1.32
3544.68	75.80	85.25	83.15	80.07	90.70	36.33	4.90	2.75	3.34	1.38	0.87	2.24	1.80
3544.81	75.93	86.92	84.71	80.53	93.00	40.44	4.59	2.84	4.68	1.12	0.67	2.09	1.32
3545.05	79.88	92.50	91.09	82.56	96.10	29.21	8.51	3.00	8.27	1.13	0.65	0.63	1.25
3545.44	77.17	88.88	86.89	81.08	94.11	36.36	6.41	3.47	6.34	1.29	0.71	1.95	1.55
3545.48	81.33	94.97	93.95	83.12	97.42	18.33	3.66	2.85	13.02	1.07	0.61	0.44	1.20
3546.19	89.49	100.00	100.00	89.49	100.00	1.99	1.69	1.24	10.04	2.41	1.57	0.03	0.33
3546.50	87.14	100.00	100.00	87.14	100.00	0.84	–	0.80	6.85	1.31	0.77	0.01	0.08
3546.95	88.08	100.00	100.00	88.08	100.00	1.06	–	0.76	2.18	1.67	0.89	0.01	0.07
3547.20	88.99	100.00	100.00	88.99	100.00	1.15	–	0.95	5.45	1.49	1.06	0.01	0.14
3547.49	90.23	100.00	100.00	90.23	100.00	3.16	–	2.18	15.57	7.46	4.30	0.04	0.48
3548.33	69.63	76.68	74.06	77.88	86.80	25.74	–	2.90	2.16	1.51	0.92	0.87	1.50
3548.72	71.80	80.12	77.51	78.83	88.96	34.42	3.14	2.69	2.65	1.36	0.87	1.47	1.75
3548.99	72.07	80.76	78.12	78.83	89.36	37.53	3.03	2.69	3.02	1.32	0.86	2.17	1.75
3549.45	71.61	80.20	77.50	78.55	89.01	37.28	2.84	2.73	2.93	1.31	0.85	2.26	1.72
3549.60	72.05	80.89	78.22	78.37	88.94	39.61	2.98	2.76	2.60	1.26	0.78	2.49	1.72
3549.71	71.00	79.63	76.81	78.09	88.66	31.55	3.10	2.73	3.53	1.67	0.72	3.49	1.43
3550.14	71.49	80.13	77.40	78.44	88.97	38.89	3.44	2.88	2.99	1.27	0.78	1.88	1.69
3550.35	73.46	82.80	80.30	79.35	90.36	40.41	3.03	2.89	3.37	1.27	0.81	2.76	1.49
3550.66	72.49	81.15	78.59	78.48	88.72	36.83	3.01	2.65	2.74	1.23	0.80	2.35	1.70
3550.75	71.99	80.20	77.65	79.01	89.01	36.52	3.27	2.59	2.86	1.35	0.85	2.37	1.57
3551.36	75.12	84.80	82.55	79.19	90.03	37.15	2.96	2.69	3.26	1.20	0.72	2.43	1.33
3552.05	76.39	87.30	85.18	80.88	93.22	39.27	5.65	2.93	5.01	1.20	0.71	2.10	1.37
3552.40	75.17	84.94	82.69	80.54	91.85	33.91	4.03	2.78	3.87	1.22	0.71	2.33	1.51
3553.25	79.01	90.95	89.34	81.58	94.36	38.49	4.72	2.83	6.21	1.14	0.63	2.64	1.22
3553.60	78.83	90.97	89.33	81.56	94.63	39.62	8.88	2.85	6.23	1.13	0.64	2.76	1.30
3554.10	79.29	91.94	90.41	81.59	95.05	41.31	8.47	2.99	7.05	1.15	0.65	3.12	1.33
3554.88	79.24	92.29	90.77	81.90	95.92	42.03	9.91	3.00	8.72	1.08	0.58	3.08	1.23
3555.25	79.26	92.21	90.69	82.01	95.95	41.01	8.31	2.97	8.18	1.07	0.59	2.93	1.28
3556.20	85.73	100.00	100.00	85.73	100.00	4.44	1.87	2.24	7.47	2.16	0.63	0.15	0.80
3556.65	79.29	91.22	89.66	82.43	95.41	35.09	–	2.67	6.71	1.20	0.67	2.45	1.66
3557.05	79.39	91.97	90.46	82.24	95.82	39.14	8.06	3.30	8.34	1.11	0.58	2.22	1.30
3558.17	76.53	86.40	84.39	81.43	92.71	36.08	7.07	2.95	4.29	1.25	0.72	3.28	1.69
3558.60	75.55	86.12	83.86	80.44	92.54	39.42	4.48	2.69	4.32	1.11	0.68	2.81	1.44
3558.85	74.88	84.94	82.60	80.20	91.85	39.83	3.50	2.62	3.89	1.86	0.76	2.57	1.51
3560.14	74.54	88.34	86.45	80.15	91.74	40.71	7.18	2.48	3.83	1.81	0.78	2.89	1.51
3561.90	75.33	90.50	88.75	81.69	95.01	40.36	5.64	2.51	6.57	1.63	0.70	2.40	1.44
3566.90	76.25	91.25	89.69	82.38	95.43	40.03	6.35	2.73	7.20	1.74	0.66	2.70	1.47
3568.91	75.99	91.95	90.37	81.82	95.81	42.28	6.75	2.79	7.89	1.57	0.64	2.65	1.50
3575.10	75.53	89.41	87.50	81.26	94.41	42.76	4.94	2.56	5.83	1.62	0.71	2.75	1.42
3577.95	76.01	86.38	84.23	79.77	91.26	41.54	4.83	2.69	3.60	1.80	0.79	2.71	1.57
3579.94	76.74	88.43	86.35	80.36	93.27	40.74	5.27	2.60	4.79	1.70	0.67	2.56	1.45
3581.96	78.49	91.23	89.53	81.57	95.41	39.69	6.27	2.79	7.18	1.60	0.74	2.52	1.38
3583.00	77.48	89.36	87.43	81.22	94.38	42.58	4.93	2.84	5.80	1.62	0.70	2.79	1.01
3584.10	74.76	85.01	82.63	80.04	91.90	20.65	4.00	2.26	3.92	2.07	0.72	0.75	1.04

in the lower part of this interval (Fig. 5).

Flood events represented by sandstones and siltstones with normally and inversely–normally graded bedding occur mainly at depths of 3517.5–3532.3 m in the upper part of unit 6 (i.e., the upper part of the Jenkyns Event) and 3564.5–3571.6 m. The interval from 3517.5 to 3532.3 m is dominated by shelly siltstones without erosional bases, indicating distal hyperpycnite. The 3564.5–3571.6 m interval is dominated by sandstones with normally and inversely–normally graded beddings and erosional bases, and it represents proximal hyperpycnite (Fig. 5).

In summary, during the Jenkyns Event, the frequency and energy of storms and floods increased significantly. It is particularly noteworthy that the lower part of the Jenkyns Event was dominated by storms and hurricanes, while the frequency of flood events increased in the upper part. The increased frequency and energy of storms and floods may indicate an intensified hydrological cycle during the Jenkyns Event and may also be associated with lake-level decline.

There was a lake transgression during the Jenkyns Event in the well LQ104X. Shallow–semi-deep lake siltstones and sandstones were deposited before the Jenkyns Event, whereas deep lake mudstones were dominated during the Jenkyns Event in the well LQ104X (Fig. 5). Therefore, higher frequency and higher energy of storm and flood events

during the Jenkyns Event would be caused by an enhanced hydrological cycle and severe stormy weather conditions.

This conclusion is confirmed by the evolution of lithofacies paleo-geography in the Sichuan Basin. In the Guangyuan area (northern Sichuan Basin), which is closer to the provenance area than the well LQ104X, a lake transgression can also be inferred by the lithological change from shore-shallow lake glutenites before the Jenkyns Event to shallow lake siltstones and sandstones during the Jenkyns Event. There might be lake regression locally in the Sichuan Basin. It is worth noting that the enhanced hydrological cycling can also be inferred in the Guangyuan area. In the proximal locality, the Guangyuan area, shallow lake siltstones and sandstones are always interbedded with diluvial fan conglomerate deposits during the Jenkyns Event (Sichuan Geology and Mineral Resources Bureau, 1991). Because the well LQ104X is farther away from the provenance and the water is deeper than that in the Guangyuan area, it is reasonable to believe that the proximal locality accumulated conglomerates while the distal locality was sandstone deposition during flooding. These diluvial fan conglomerates probably correspond to flood deposits in the well LQ104X, which are all caused by floods and enhanced hydrological cycling in the Jenkyns Event.

Table 4

Element ratios for weathering, paleoclimate, and hydrological cycling of 122 samples from 3490 m to 3585 m in the well LQ104X in the Sichuan Basin.

Depth	K/Na	10,000 × K/Ti	Rb/Ti	Cs/Ti	Fe/Mn	Th/U	Na/Ti	10,000 × Rb/K
3490.2	2.78	4.09	235.17	15.32	92.12	4.51	1.47	57.50
3491.9	3.71	4.65	274.91	17.75	126.94	5.84	1.25	59.13
3494	4.00	4.83	277.59	18.45	30.26	2.68	1.21	57.50
3496.6	2.37	4.26	228.57	15.05	83.38	3.68	1.80	53.61
3498.81	1.93	3.60	180.70	11.54	151.92	5.00	1.86	50.24
3499.6	5.61	6.00	367.61	24.85	208.84	5.30	1.07	61.27
3500.78	3.45	4.98	264.42	17.14	48.26	5.31	1.44	53.14
3502.6	3.81	5.71	324.79	20.58	81.68	4.48	1.50	56.93
3502.95	3.85	5.87	336.32	20.58	93.10	3.81	1.52	57.25
3504.5	1.64	3.97	201.72	13.10	6.79	5.45	2.41	50.87
3505.25	3.95	6.35	364.13	23.59	80.00	3.15	1.61	57.36
3508.25	2.61	4.82	251.63	15.31	137.00	5.18	1.84	52.25
3510.6	1.08	3.03	143.13	7.78	49.02	4.09	2.81	47.22
3512.6	4.95	5.24	314.24	20.57	122.02	4.45	1.06	59.93
3513.52	4.78	5.52	317.31	20.48	78.31	4.77	1.15	57.49
3514.59	4.56	5.50	312.62	20.49	134.66	4.77	1.20	56.89
3515.52	5.94	6.91	419.46	27.74	107.80	4.20	1.16	60.68
3516.3	2.34	4.22	236.40	14.24	108.68	5.05	1.80	56.00
3517.12	1.50	3.20	150.53	10.09	72.64	4.90	2.14	47.07
3518.85	3.00	3.25	166.27	10.48	10.36	3.64	1.08	51.11
3519.72	6.00	6.73	401.60	25.97	148.64	4.66	1.12	59.69
3521.15	5.98	7.35	433.87	30.05	74.96	3.16	1.23	58.99
3522.27	1.95	3.97	227.01	13.70	72.01	4.03	2.04	57.14
3523	7.32	8.55	521.37	31.05	112.90	4.39	1.17	61.00
3523.29	2.86	4.90	280.65	17.66	26.75	3.75	1.72	57.22
3524.2	6.02	6.86	433.94	26.77	194.14	4.94	1.14	63.29
3524.7	7.14	7.42	458.94	29.23	107.62	4.78	1.04	61.89
3525.28	2.17	4.53	250.29	16.89	39.71	3.22	2.09	55.19
3525.8	6.12	7.64	447.12	28.00	217.62	4.40	1.25	58.49
3526.01	7.02	8.37	516.84	32.90	259.79	4.96	1.19	61.76
3526.76	2.83	4.47	240.55	16.19	31.30	2.70	1.58	53.85
3527.15	7.14	8.82	538.79	32.90	142.23	4.73	1.24	61.07
3527.5	4.68	5.89	359.86	24.47	127.94	4.42	1.26	61.09
3528.55	2.78	4.85	281.88	17.81	56.19	3.08	1.74	58.06
3529.4	6.76	8.15	471.85	30.29	205.39	4.21	1.21	57.89
3530.5	5.13	6.69	407.00	27.17	164.22	4.32	1.30	60.83
3531.28	3.62	5.52	329.55	21.95	45.96	4.08	1.53	59.71
3531.85	3.91	5.57	335.11	21.49	201.61	4.68	1.43	60.11
3532.38	4.28	6.06	375.87	23.67	189.02	4.71	1.42	62.07
3532.98	4.62	6.23	375.80	24.20	163.49	4.14	1.35	60.31
3533.35	6.00	8.81	555.08	35.31	199.53	4.54	1.47	62.98
3534.27	3.08	5.07	278.15	19.01	43.68	2.99	1.64	54.89
3534.8	5.75	8.06	506.74	33.02	190.52	4.22	1.40	62.88
3535.15	6.16	9.26	579.65	39.38	198.08	3.97	1.50	62.58
3535.56	6.21	9.61	613.10	39.58	221.57	3.68	1.55	63.78
3536.3	5.79	8.82	554.60	35.92	229.08	3.71	1.52	62.87
3536.48	5.58	7.38	450.33	30.53	99.73	4.04	1.32	60.99
3536.68	8.97	8.11	527.13	35.79	87.45	4.45	0.90	64.97
3537.05	3.16	5.07	310.78	20.30	205.58	3.94	1.61	61.31
3537.7	5.14	6.72	413.37	27.51	146.52	3.91	1.31	61.54
3538.18	6.55	8.09	542.65	33.82	197.99	3.75	1.24	67.09
3538.25	3.87	5.62	345.65	22.69	135.28	3.34	1.45	61.50
3538.35	6.47	8.61	562.32	35.84	250.00	3.88	1.33	65.30
3538.51	6.83	8.40	549.74	34.82	257.69	3.79	1.23	65.42
3539.45	6.71	7.80	490.52	31.99	195.26	3.86	1.16	62.92
3539.75	5.42	5.66	370.56	26.10	100.55	4.65	1.04	65.50
3539.9	5.33	5.70	370.37	24.38	191.44	4.76	1.07	64.98
3539.95	6.89	8.85	576.39	39.41	122.80	3.28	1.28	65.10
3540.45	6.32	8.37	541.57	36.45	36.47	4.29	1.33	64.68
3540.64	3.03	4.63	289.26	18.43	125.41	4.57	1.53	62.50
3540.75	5.98	7.92	490.54	34.86	134.81	3.95	1.32	61.95
3541.05	5.42	6.20	386.61	26.57	180.46	4.35	1.14	62.37
3541.44	6.28	7.00	457.63	28.21	173.45	3.97	1.11	65.40
3542.46	3.33	3.23	190.32	12.90	36.70	2.55	0.97	59.00
3542.52	5.25	4.04	219.23	15.19	45.58	3.13	0.77	54.29
3542.6	3.49	4.52	270.17	18.95	122.74	4.87	1.29	59.75
3542.65	4.06	4.97	302.91	20.78	78.80	4.75	1.22	60.94
3542.85	3.01	4.11	243.64	16.49	109.39	4.68	1.36	59.29
3542.9	4.21	5.31	321.90	22.08	115.61	4.70	1.26	60.63
3543.1	3.85	4.73	298.88	18.99	135.00	5.06	1.23	63.19
3543.86	2.03	3.53	188.11	12.04	104.94	4.55	1.74	53.23
3544.05	8.25	8.01	549.87	36.39	182.33	4.24	0.97	68.69
3544.21	7.85	7.76	553.78	34.16	187.55	3.84	0.99	71.35
3544.38	8.22	7.81	532.98	35.09	194.95	4.09	0.95	68.24

Table 4 (*continued*)

Depth	K/Na	10,000 × K/Ti	Rb/Ti	Cs/Ti	Fe/Mn	Th/U	Na/Ti	10,000 × Rb/K
3544.5	8.31	7.57	541.77	33.80	238.83	4.31	0.91	71.57
3544.53	7.33	6.91	478.26	31.28	185.24	4.35	0.94	69.23
3544.6	7.77	7.48	511.11	32.72	200.51	4.80	0.96	68.32
3544.65	6.95	7.09	481.68	29.71	124.00	4.98	1.02	67.90
3544.68	2.33	3.74	222.33	14.67	146.55	4.90	1.61	59.41
3544.81	4.02	5.12	319.72	21.12	131.27	4.52	1.27	62.45
3545.05	7.00	6.06	394.03	27.64	80.84	4.76	0.87	65.02
3545.44	4.73	5.02	340.63	22.08	117.86	4.87	1.06	67.84
3545.48	8.18	7.81	507.30	35.96	54.87	3.13	0.96	64.96
3546.19	4.00	2.58	148.39	10.97	19.63	4.19	0.65	57.50
3546.5	5.00	3.85	246.15	17.69	22.97	3.25	0.77	64.00
3546.95	1.25	2.78	194.44	11.67	7.96	3.29	2.22	70.00
3547.2	3.50	3.68	194.74	14.21	18.95	2.71	1.05	52.86
3547.49	2.00	2.35	152.94	8.24	16.12	3.82	1.18	65.00
3548.33	1.37	3.05	187.46	11.48	28.74	4.37	2.22	61.50
3548.72	1.88	3.69	216.11	13.94	46.08	5.02	1.97	58.55
3548.99	2.20	3.99	227.37	15.37	66.26	4.76	1.81	57.03
3549.45	2.14	4.04	233.33	15.42	60.78	4.91	1.89	57.69
3549.6	1.98	4.07	244.96	15.34	102.64	5.09	2.06	60.15
3549.71	2.24	4.15	261.30	15.78	81.86	5.34	1.85	63.03
3550.14	2.26	4.00	244.42	15.74	46.51	5.25	1.76	61.17
3550.35	2.55	4.64	272.23	17.85	81.97	4.67	1.82	58.64
3550.66	2.14	3.82	219.61	14.92	70.94	5.14	1.78	57.44
3550.75	2.03	3.54	210.00	13.66	57.87	4.74	1.74	59.32
3551.36	2.59	3.98	248.58	15.01	76.42	5.19	1.54	62.38
3552.05	4.00	4.51	286.81	18.32	67.77	5.17	1.13	63.56
3552.4	3.03	3.83	245.63	15.17	64.72	5.10	1.26	64.21
3553.25	5.22	5.01	337.57	21.23	37.15	5.61	0.96	67.38
3553.6	5.30	5.12	338.80	21.14	99.53	5.52	0.97	66.23
3554.1	5.89	5.46	361.90	22.08	97.12	5.63	0.93	66.24
3554.88	7.76	6.61	461.88	27.35	66.85	5.57	0.85	69.83
3555.25	7.30	6.40	435.31	26.97	70.40	5.45	0.88	67.98
3556.2	6.60	7.42	479.78	31.35	25.14	3.23	1.12	64.70
3556.65	5.36	5.16	347.48	21.44	66.62	5.39	0.96	67.33
3557.05	7.18	6.52	468.97	26.49	58.84	5.60	0.91	71.98
3558.17	3.30	4.53	295.22	18.40	81.26	4.86	1.37	65.14
3558.6	3.72	5.33	325.48	20.90	107.42	4.81	1.43	61.04
3558.85	3.03	4.13	249.16	16.36	98.44	4.91	1.36	60.29
3560.14	2.98	4.11	242.41	16.05	130.10	5.04	1.38	58.98
3561.9	5.56	5.37	325.16	22.53	87.44	5.20	0.97	60.51
3566.9	5.89	5.69	381.60	26.94	137.80	5.14	0.97	67.02
3568.91	6.93	7.25	465.77	33.18	128.07	5.23	1.05	64.27
3575.1	4.92	6.11	365.80	25.69	117.53	4.98	1.24	59.84
3577.95	2.80	3.99	232.39	15.64	104.19	4.86	1.42	58.20
3579.94	4.06	5.29	331.56	22.73	77.14	4.56	1.30	62.66
3581.96	6.29	7.47	415.57	30.86	106.06	4.48	1.19	55.60
3583	4.90	5.83	353.68	24.97	115.80	4.54	1.19	60.64
3584.1	3.11	4.42	276.07	17.56	14.77	4.52	1.42	62.50

5.2. Continental weathering and paleoclimate

5.2.1. Sediment provenance, recycling, sorting, and diagenetic alteration

Sediment provenance (Újvári et al., 2014), recycling (Mongelli et al., 2006; Guo et al., 2018), hydraulic sorting (Bauluz et al., 2000; Bouchez et al., 2011), and diagenetic alteration (Goldberg and Humayun, 2010; Andò et al., 2012) can all affect chemical weathering indices. Chemical weathering indices based on the element geochemistry of siliciclastic sediments are only reliable if the aforementioned processes can be accounted for (Das et al., 2006; Singh, 2009; Garzanti and Resentini, 2016).

The 122 analyzed samples were divided into three groups based on their whole-rock geochemical compositions (SF. 1). Group I and II (*n* = 108) samples are similar in geochemical compositions, except that the Ca and Sr contents of group II samples are higher than those of group I samples. This indicates that these two groups may have had the same provenance. The higher Ca and Sr contents of group II samples may be related to their slightly higher carbonate contents, which is consistent with microscopic observations. The total REE contents and REE patterns of group I and II samples are similar to those of the SQ, UCC, and Yangtze Craton (SF. 2), which also indicate that the provenance of both these samples was the same. A significant difference in elemental composition

is related to the high shell contents of group III samples. High carbonate contents result in much higher Ca and Sr, lower REE, and more depleted heavy REE contents (Kamber and Webb, 2001). This reflects the dilution effect of the carbonate material. As such, the 122 samples may all have had the same provenance.

Thorium and Sc are often used for tracing sediment provenance because both are immobile elements during erosion, transport, and deposition (Cullers et al., 1988, Cullers, 2002). The studied samples exhibit minor variations in Th/Sc ratios, and the average Th/Sc ratio is similar to those of the SQB and Yangtze Craton. This conclusion is consistent with the inferences from the REE data (Fig. 6a).

Data for samples with low carbonate contents and no evidence of hydraulic sorting were selected to construct plots of $R^{3+}/(R^{3+} + R^{2+} + M^+) - \Delta 4Si\%$ ($M^+ = Na^+ + K^+ + 2Ca^{2+}$; $R^{2+} = Fe^{2+} + Mg^{2+}$; $R^{3+} = Al^{3+} + Fe^{3+}$; Meunier et al., 2013) and A–CN–K (Fedo et al., 1995; Cullers and Podkovyrov, 2000). In both diagrams, the samples trace a weathering trend of mafic rocks to the SQ (Fig. 6b, c). This inference is supported by the lithofacies and paleogeography. In fact, the Qinling orogenic belt outcrops large volume of mafic rocks including gabbro, biotite-hornblende-granite, biotite-bearing granite and plagioclase granite in the South Qinling, and mafic dike swarms are distributed in North Daba Mountain (Fig. 1). Previous studies have shown that the paleocurrent
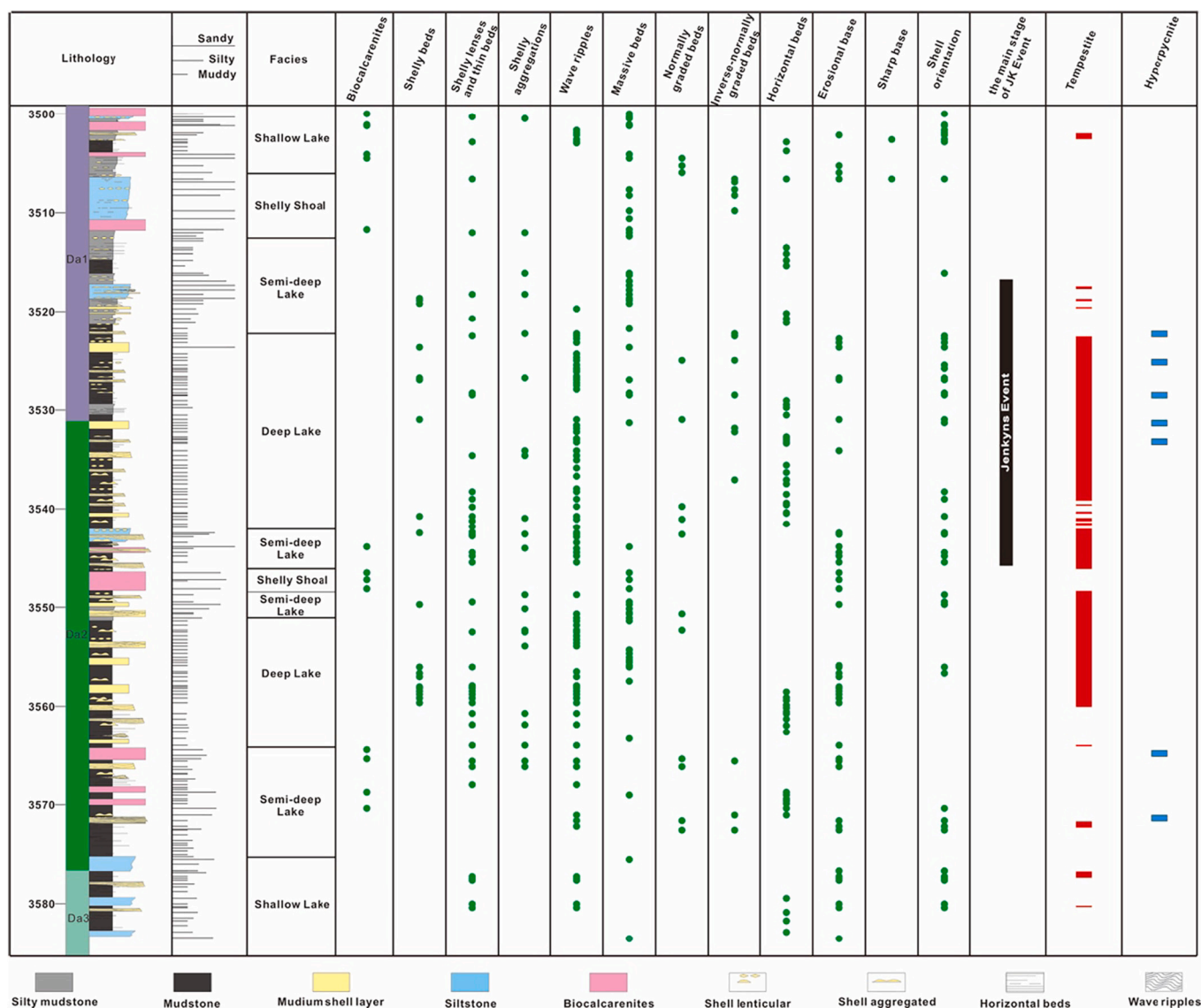
Fig. 5. Development of tempestites and hyperpycnites from 3490 m to 3585 m in the Da'anzhai Member in the well LQ104X based on sedimentary statistic data.

directions in the Zhenzhuchong Formation were to the south and southwest (Cheng, 2014). During the deposition of the Da'anzhai Member, the tectonism was calm, and the landforms inherited those of the Zhenzhuchong Formation. The Qinling orogenic belt had a higher terrain and was closer to the study area, and was likely the sediment provenance at this time.

The Zr/Sc–Th/Sc diagram is widely used to investigate sedimentary recycling (McLennan et al., 1993). The studied samples plot along the first-cycle weathering line and far from the sedimentary recycling line (Fig. 7a). In addition, sedimentary recycling accumulates stable and erosion-resistant minerals, which causes WIP values to decrease linearly, whereas CIA, CIX, α_E^{Al}, and other indices are unaffected (Garzanti et al., 2013a; Garzanti and Resentini, 2016). Therefore, there are no negative linear correlations between CIA, CIX, and WIP values if sedimentary recycling occurs. For the studied samples, there is a clear linear correlation between the CIA and other chemical weathering indices. The correlation coefficient between the CIX and WIP values is 0.69, indicating that most samples were first-cycle sediments (Fig. 7b; Garzanti et al., 2013b, 2014a). However, there are 17 samples that may have been affected by hydraulic sorting (Fig. 7b).

The Al/Si ratio is widely used to constrain the hydraulic sorting of sediments (Bouchez et al., 2011; Guo et al., 2018). The samples with a

negative linear correlation between CIX and WIP values have an average molar Al/Si ratio of 0.41, with a standard deviation of 0.03. However, for those samples that do not plot on the linear correlation, the average ratio is 0.28 and the standard deviation is 0.05. The Al/Si ratios show that the samples with no relationship between CIX and WIP values are coarse, indicating that these samples were affected by hydraulic sorting. For the first-cycle samples, the correlation coefficients between Al/Si ratios and CIX and WIP values are 0.21 and 0.01, respectively, indicating that the chemical weathering indices of these samples are unaffected by hydraulic sorting (Fig. 7c). However, the other samples have correlation coefficients of 0.92 and 0.84, respectively, indicating that hydraulic sorting has affected the chemical weathering indices (Fig. 7d).

The diagenetic alteration, particularly illitization, can significantly alter the chemical weathering index values (Fedo et al., 1995). Our samples define a trend parallel to the A–CN boundary on an A–CN–K ternary diagram, indicating that these samples were not affected by illitization (Fig. 5c; Fedo et al., 1995). Furthermore, diagenetic alteration produces a weak linear relationship between chemical weathering indices. However, there are strong linear relationships between the different chemical weathering indices, indicating that post-depositional diagenetic alteration had little effect on the indices (SF. 3). In addition, the organic matters of the Da'anzhai Member in the study area have a
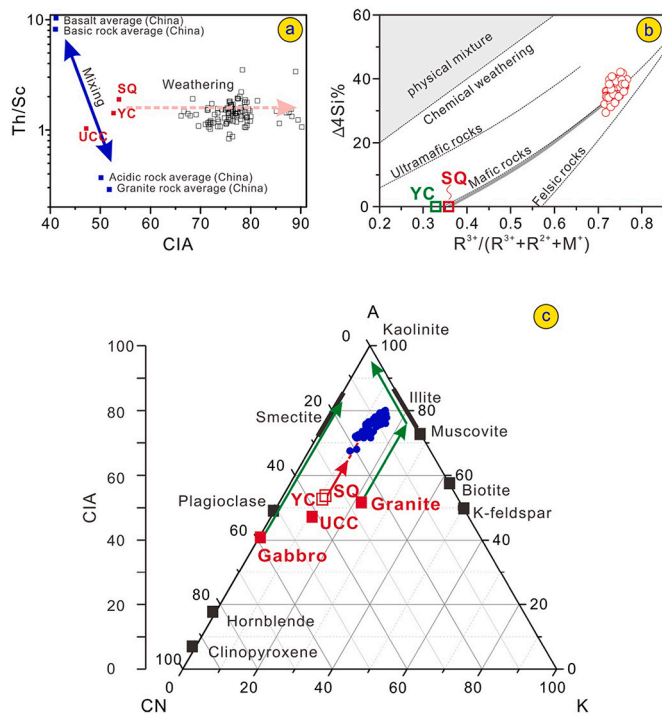
Fig. 6. a) CIA-Th/Sc plot showing the SQ and YC may be the provenance, and no linear correlation between Th/Sc and CIA indicating that the provenance did not affect the CIA. b) $R^{3+}/(R^{3+}+R^{2+}+M^+)$-$\Delta 4Si\%$ plot confirming that the SQ should be provenance ($M^+ = Na^+ + K^+ + 2Ca^{2+}$; $R^{2+} = Fe^{2+} + Mg^{2+}$; $R^{3+} = Al^{3+} + Fe^{3+}$); c) A-CN-K plot showing that the weathering tracks the weathering trend of plutonic rocks based on thermodynamic calculations to the SQ. SQ: the South Qinglin Upper Crust; YC: the Yangtze Upper Crust; UCC: the Upper Continental Crust.

moderate thermal maturity with Ro ranging from 0.8% to 1.0% (Sun et al., 2021). The alternation of kaolinite to illite occurs commonly at 120–140 °C that correspond roughly to 4000 m of burial depth (Bjørlykke and Aagaard, 1992; Kozłowska and Poprawa, 2004). It is likely, therefore, that burial diagenesis had a limited impact on transforming the initial kaolinite into illite and/or chlorite.

In summary, the provenance region of the studied samples was the SQ. Sedimentary recycling and post-depositional diagenetic alteration had negligible effect on the chemical weathering indices, and only 17 samples were affected by hydraulic sorting.

5.2.2. Weathering

There is a marked linear correlation between the CIA and other chemical weathering indices, such as the WIP, CIW, PIA, and α_E^{Al} (SF. 3), and the CIA is widely used to quantify the intensity of chemical weathering (Li and Yang, 2010). CIA values are mainly 66–80, indicating that the provenance area underwent moderate chemical weathering. Based on the CIA values, the interval at depths of 3490–3585 m in the well LQ104 can be divided into nine units. The odd-numbered units have relatively low CIA values, and the even-numbered units have high CIA values (Fig. 8, the value of the auxiliary line is 77.5). There is a very short interval of weak chemical weathering (unit 5) sandwiched between two protracted intervals of intense chemical weathering (units 4 and 6; 3520–3546.1 m; Fig. 8). This protracted interval corresponds to the Jenkyns Event and the main negative CIE (Liu et al., 2020). There is another intense chemical weathering interval (unit 2) at depths of 3550.9–3558.9 m, which might correspond to the Pl-To NCIE. Further research is required.

Elemental ratios, including K/Na, K/Ti, Rb/Ti, and Cs/Ti, were also used to investigate the chemical weathering. High K/Na ratio is a typical characteristic of intense chemical weathering (White et al., 1999). The

alkali elements (Na, K, Rb, and Cs) can be absorbed by clay minerals, whereas Ti is primarily concentrated in heavy minerals (Jenny, 1932; Bouchez et al., 2011). Therefore, higher ratios indicate more intense chemical weathering. Similar to the CIA values, the 3490–3585 m depth interval of the well LQ104 can be divided into nine units based on the K/Ti, Rb/Ti, and Cs/Ti ratios. Unit 6 has higher ratios than units 2 and 4. In addition, the upper part of unit 6 has lower ratios than the lower part of unit 6 and units 2 and 4 (Fig. 8).

To further characterize the changes in the intensity of chemical weathering of each unit, particularly during and around the Jenkyns Event, Rb/K and Na/Ti ratios were used to investigate subtle changes. With intensified chemical weathering, K is preferentially leached because the ionic radius of K is smaller than that of Rb, which increases the residue Rb/K ratio (Sawyer, 1986; Perri, 2018). Sodium is a highly soluble element, and thus the Na contents of sedimentary rocks reflect the residual albite content after weathering. Therefore, a lower Na/Ti ratio indicates more intense chemical weathering. Units 2 and 4 have higher Rb/K and lower Na/Ti ratios than the upper part of unit 6, reflecting more intense chemical weathering recorded by units 2 and 4 (Fig. 8). This is consistent with the inferences drawn from the K/Na, K/Ti, Rb/Ti, and Cs/Ti ratios and CIA (Fig. 8).

The clay minerals are also important chemical weathering proxies. The content of chlorite in the samples is higher than that of kaolinite (Fig. 8). This should be related with the large volume of mafic rocks in the SQ. Weathering of mafic rocks can result in relatively low kaolinite content but high content of chlorite (Nesse, 2012). However, the kaolinite/ (illite + chlorite) ratio in the well LQ104X is similar to the change tendency of the chemical weathering indices above-mentioned. Kaolinite reflects intense chemical weathering in tropical or humid-subtropical climates (Singer, 1984; Hallam, 1984). Illite develops as a result of decreased hydrolytic processes in continental weathering under cool and/or arid climate conditions (Singer, 1984; Chamley and Pierre, 1984). A cool condition leads to increased chlorite content (Weaver, 1989). As discussed above, the protolith of source area also controls the content of minerals, however, the SQ is the primary source area during the deposition of the Da'anzhai Member. Therefore, higher kaolinite/ (illite + chlorite) ratios indicate more intense chemical weathering. The expected distinct correlation between geochemical and mineralogical indices is observed (Fig. 8). The upper part of unit 6 has a lower K/ (I + C) ratio than that of the lower part of unit 6 and units 2 and 4.

5.2.3. Paleoclimate

The intensity of chemical weathering depends mainly on climate, and warm and humid conditions lead to intensified chemical weathering. The Th/U and Fe/Al ratios are widely used as paleoclimate proxies. Low Th/U and high Fe/Al ratios indicate a humid climate (Liu et al., 2007; Pattan et al., 2012; Delpomdor et al., 2013; Gould et al., 2014). U is considered to be more soluble than Th. Thus high Th/U ratio in sediments can reflect humid climates and palaeoclimates (Ruffell and Worden, 2000). Th/U ratios in sediments increase with intensified weathering due to oxidation and loss of uranium(McLennan et al., 1993). The changes in Fe/Al ratio in the sediments have been related to varying sediment flux controlled by the rainfall changes (Lamy et al., 2000; Dezileau et al., 2007). Therefore, the higher Fe/Al ratio indicates more rainfall. Units 4 and 6 have high Th/U ratios indicating a humid climate during the Jenkyns Event. The Fe/Al ratios also show a similar trend of Th/U but have higher values in the upper part of unit 6 than those in the lower part of unit 6 and units 2 and 4, which suggests that there was more rainfall in the upper part of unit 6 (Fig. 8). Vander-averoet and Deconinck (1997) considered the mixed layer illite/smectite to reflect a warm and seasonally humid climate. However, there is no significant difference between the average values of the mixed layer illite/smectite of units 2, 4, and 6, indicating that the more rainfall in the upper part of unit 6 is not seasonal. The climate in the Sichuan Basin is different from the Qaidam Basin (Lu et al., 2020). The reason might be that the Sichuan Basin is near to the Tethys Ocean, however, the Qaidam
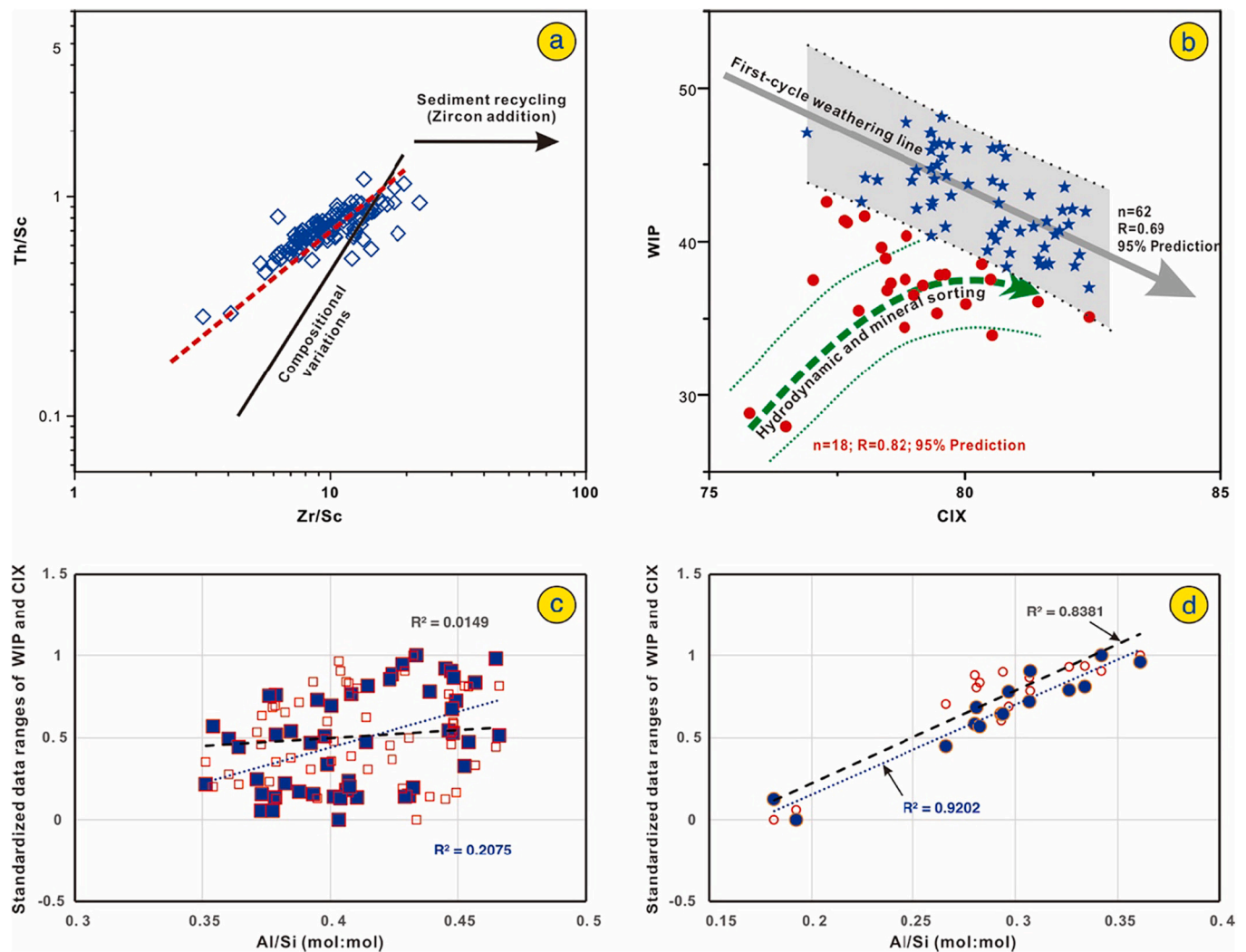
Fig. 7. a) Zr/Sc-Th/Sc plot showing that all the samples fall along the first-cycle weathering line, far from the sedimentary recycling. Elevated Th/Sc ratios may be related to the high evolution for the SQ; b) CIX-WIP plot showing that samples with low carbonate content fall along the first-cycle weathering line, whereas some samples fall along the hydrodynamic and mineral sorting line. Blue stars are samples with low carbonate content; red dots are remainder samples. Relationship between chemical weathering indices WIP and CIX and hydrodynamic sorting index Al/Si molar ratio showing no relationship for the sample with low carbonate content (c) but a significant linear relationship for samples affected by hydraulic sorting (d). (For interpretation of the references to colour in this figure legend, the reader is referred to the web version of this article.)

Basin is an inland lake. Therefore, the humid-arid cycle is not obvious in the Sichuan Basin.

5.3. Enhanced continental weathering and hydrological cycling during the Jenkyns Event

5.3.1. Enhanced hydrological cycling and its effects on continental weathering

In general, wetter and warmer conditions lead to enhanced chemical weathering. In particular, unit 6 corresponds to the Jenkyns Event (Liu et al., 2020), which was an interval of high temperatures (McArthur et al., 2000; Dera et al., 2009; Suan et al., 2010) and a humid climate as discussed above. Theoretically, the chemical weathering recorded by unit 6 should be more intense than that of the other units. However, the chemical weathering of the upper part of unit 6 is weaker than those of units 2 and 4 (Fig. 8). This might reflect the effects of the transportation rates on the chemical weathering intensity (West et al., 2005; Gabet and Mudd, 2009; Brański, 2012). If the rate of material being transported out of the source area by a river is slow, then source rocks will undergo protracted chemical weathering. In this case, the calculated weathering

indices record intense chemical weathering. If the source rocks are exposed to only a short interval of chemical weathering due to rapid transport out of the source area, then the calculated weathering indices record weak chemical weathering, even in a warm and humid climate. Therefore, the weaker chemical weathering indices recorded by the upper part of unit 6 may be related to enhanced hydrological cycling, and sediment transportation rate out of the source area. It is similarly to the case observed in coeval sediments in the Polish Basin (Brański, 2012).

A sedimentological study supported this conclusion. In the upper part of the Jenkyns Event, many thin, homogeneous, fluidized mud layers formed by hyperpycnal currents, and the more common and thicker siltstones in the upper part of unit 6 indicate that river discharge increased during this interval. The increased content of plant fragments in the sediments due to the increase in river discharge is also observed (Fig. 4k, l). In addition to the hyperpycnites, tempestites are also common in unit 6. Therefore, it is reasonable to infer that enhanced hydrological cycling during the upper part of the Jenkyns Event reduced the intensity of chemical weathering.

Geochemical results show that Fe/Al ratio is significantly higher in
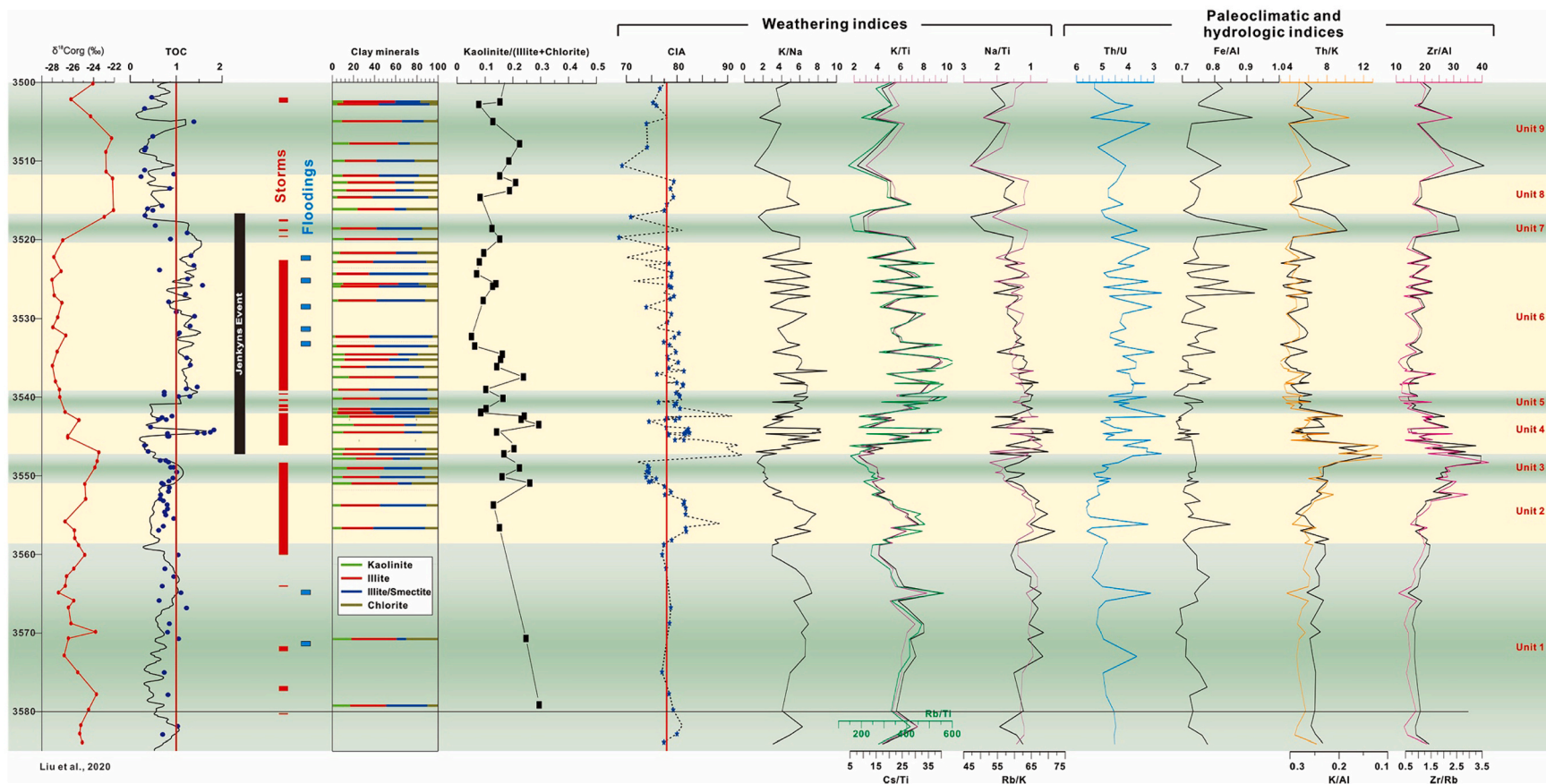
Fig. 8. Clay mineral content, weathering intensity, and paleoclimate during the Jenkyns Event. $\delta^{13}C_{org}$ curve referring to Liu et al., 2020; the blue dots for TOC are the measured values, and the line for TOC is calculated based on log data; the blue stars for CIA are the samples with low carbonate content and free hydrodynamic sorting. (For interpretation of the references to colour in this figure legend, the reader is referred to the web version of this article.)

the upper part of unit 6, suggesting more rainfall (Fig. 8). Increased rainfall will lead to faster denudation and transportation. In addition, the clay mineral composition can also provide some valuable clues. For example, there is a relatively low kaolinite content in the upper part of unit 6. Three possible reasons for this phenomenal: 1) due to the strong hydrological cycle, the denuded rocks are transported away from the weathering area before thorough chemical weathering. So that the kaolinite content is not high. 2) It is related to the transportation way of clay minerals. Compared with illite, kaolinite is settled closer to the source. Therefore, as the lake level rises during the Jenkyns Event, the content of kaolinite will also decline (Chamley, 1989; Pellenard and Deconinck, 2006; Godet et al., 2008). 3) The mafic rocks in the source area (the South Qinling) may lead to reduce the kaolinite content. However, during the whole Jurassic, the South Qinling is the primary provenance. Therefore, we believe that the rising lake-level super-imposed on the enhanced hydrological cycle led to the decline of kaolinite content in the upper part of unit 6. The decrease in kaolinite content may also be associated with hot and less humid conditions that somewhat restrain chemical weathering (Brański, 2012).

5.3.2. Correlation with marine records and the response to the Jenkyns Event

A stratigraphic correlation between the well LQ104X and the La Herradura section in Spain, based on organic carbon isotope curves, shows that the intensified chemical weathering during the Jenkyns Event coincided with high sea-surface temperatures (Fig. 9). Higher temperatures enhanced the intensity of chemical weathering. Previous studies have shown that the decomposition rate of minerals follows the Arrhenius equation and that the effect of temperature on weathering rate follows an exponential law (White and Blum, 1995; Dessert et al., 2003). In fact, intensified continental weathering and high temperatures

during the JE have been recorded in marine and marginal-marine strata (Hesselbo and Pieńkowski, 2011; Brański, 2012; Pieńkowski et al., 2016, 2020; Ruebsam et al., 2020). Suan et al. (2008) proposed that the seawater temperature in the Early Toarcian increased by 7 °C for 900 kyr. This indicates that the higher temperature during the JE affected the intensity of the chemical weathering of the continents.

Furthermore, Ruebsam et al. (2020) suggested that the sea surface temperature was high throughout the JE, and there were four short low-temperature intervals in the Toarcian. Our study also identified four intervals of weak chemical weathering. Moreover, Pieńkowski et al. (2016, 2020) also showed several (4–5) similar temperature steps in Lower Toarcian of Poland. Furthermore, each interval of intensified chemical weathering was followed by an interval of weak chemical weathering, similar to the changes in sea surface temperatures (Fig. 9). This periodic cooling may have been due to the negative feedback of chemical weathering, as intensified chemical weathering consumes atmospheric CO_2 and leads to cooling (Cohen et al., 2004; Percival et al., 2016; Kemp et al., 2020). Large amounts of organic matter burial lead to a reduction in atmospheric CO_2, which can also lead to global cooling (Berner, 2003). Xu et al. (2017) suggested the burial of ~460 Gt organic carbon in the Sichuan Basin alone, which may also be an essential possibility.

Previous studies of marine strata have suggested that enhanced hydrological cycling occurred during the JE, and our study has also shown that there were more tempestites, hurricane deposits, and hyperpycnites during the Jenkyns Event (Fig. 9). This conclusion is consistent with the evidence from the Portugal Peniche marine profile (Hesselbo et al., 2007), the Japanese marine profile (Izumi et al., 2018), the British Cardigan Bay Basin marine profile (Xu et al., 2018), the British Cleveland Basin marine profile (Slater et al., 2019) and the marginal-marine profile from Poland (Leonowicz, 2011). The high temperatures not only
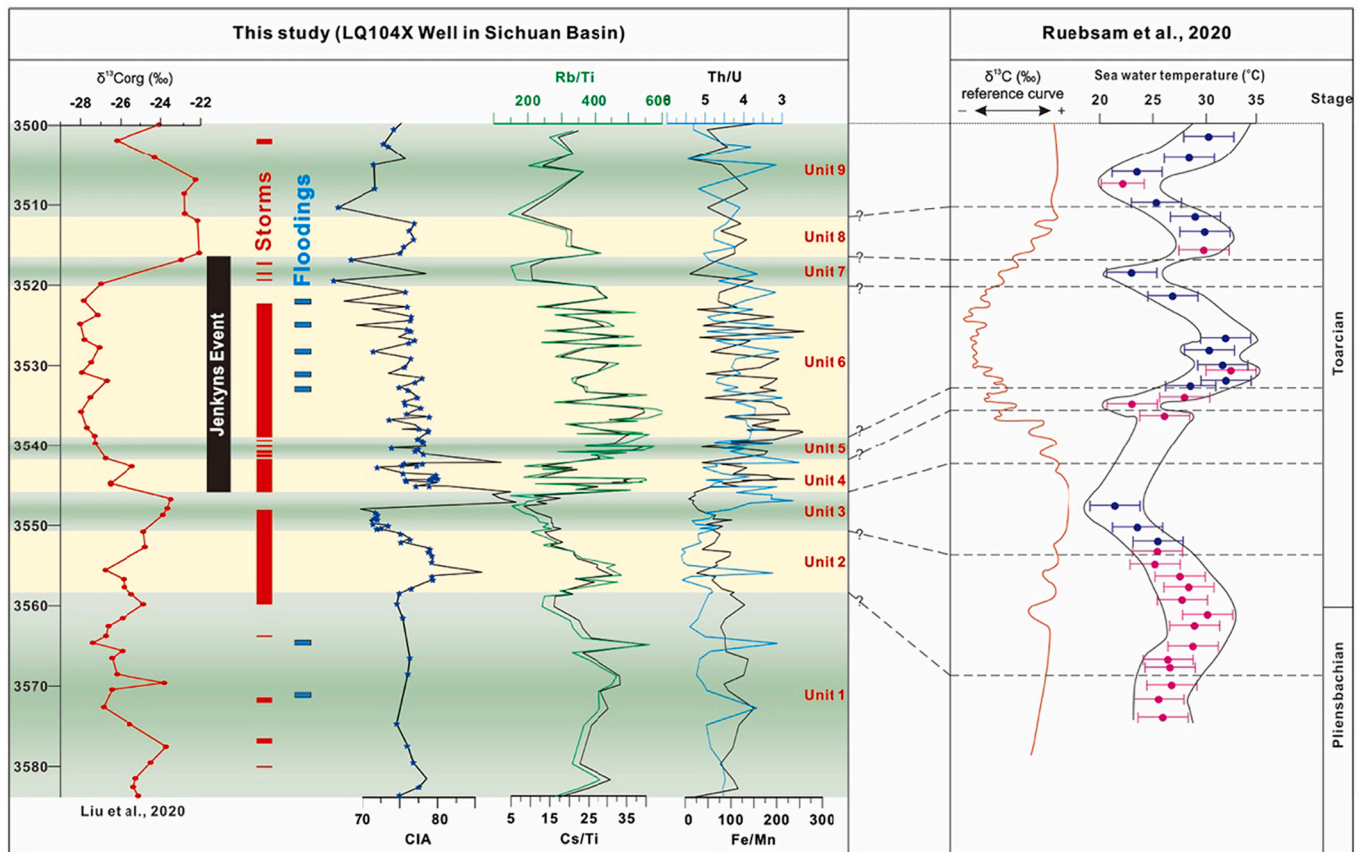
Fig. 9. Correlation between weathering intensity, paleoclimate, and hydrological cycling recorded in the well LQ104X and surface seawater temperature. Surface seawater temperature curve referring to Ruebsam et al., 2020.

increased the intensity of chemical weathering but also generated atmospheric water vapor, which led to extreme weather phenomena such as storms and floods. In general, when a storm reaches landfall, its energy decreases rapidly due to the limited supply of water vapor, as such, the storm develops mainly in the coastal zone (Krencker et al., 2015). Two conditions are required for storms to reach inland areas: high temperatures and an ample supply of water vapor. Our data from the well LQ104X suggest that it was humid and warm during the Jenkyns Event, which provided the excess water vapor that allowed storms to move inland. In summary, the high temperatures during the Jenkyns Event have caused enhanced hydrological cycling, an increased frequency of storms and floods, and intensified continental weathering.

6. Conclusions

(1) Bioclastic limestones and shell-rich mudstones in the Da'anzhai Member in the well LQ104X (3517.5–3546.1 m) represent tempestite deposits formed by storms and hurricanes. Siltstones and sandstones with normally and inversely–normally graded beddings are hyperpycnites related to flooding events. Tempestites and hyperpycnites were dominantly deposited during the Jenkyns Event.

(2) Multiple weathering and paleoclimatic indices and the sedimentary structures suggest that intensified continental weathering, enhanced hydrological cycling, and a humid climate characterized the Jenkyns Event.

(3) The high temperatures in the Jenkyns Event would have caused the enhanced hydrological cycling, increased frequency of storms and floods, and intensified continental weathering.

Supplementary data to this article can be found online at https://doi.org/10.1016/j.gloplacha.2022.103915.

Declaration of Competing Interest

We declare that we have no financial and personal relationships with other people or organizations that can inappropriately influence our work, there is no professional or other personal interest of any nature or kind in any product, service and/or company that could be construed as influencing the position presented in, or the review of, the manuscript entitled, "Enhanced hydrological cycling and continental weathering during the Jenkyns Event in a lake system in the Sichuan Basin, China".

Data availability

I have shared the link to my data at the Attach File step

Acknowledgments

References

Andò, S., Garzanti, E., Padoan, Limonta, M., 2012. Corrosion of heavy minerals during weathering and diagenesis: a catalog for optical analysis. Sediment. Geol. 280, 165–178. https://doi.org/10.1016/j.sedgeo.2012.03.023.

Bauluz, B., Mayayo, M.J., Fernandez-Nieto, C., Lopez, J.M.G., 2000. Geochemistry of Precambrian and Paleozoic siliciclastic rocks from the Iberian Range (NE Spain): implications for source-area weathering, sorting, provenance, and tectonic setting. Chem. Geol. 168 (1–2), 135–150. https://doi.org/10.1016/S0009-2541(00)00192-3.

Berner, R.A., 2003. The long-term carbon cycle, fossil fuels and atmospheric composition. Nature 426 (6964), 323–326. https://doi.org/10.1016/S0009-2541(00)00192-3.

Bjørlykke, K., Aagaard, P., 1992. Clay Minerals in North Sea Sandstones. https://doi.org/10.2110/pec.92.47.0065.

Bouchez, J., Gaillardet, J., France-Lanord, C., Maurice, L., Dutra-Maia, P., 2011. Grain size control of river suspended sediment geochemistry: clues from amazon river depth profiles. Geochem. Geophys. Geosyst. 12 (3) https://doi.org/10.1029/2010GC003380.

Brański, P., 2012. The mineralogical record of the early Toarcian stepwise climate changes and other environmental variations (Ciechocinek Formation, Polish Basin). Volumina Jurassica. 10 (1), 1–24.

Buggle, B., Glaser, B., Hambach, U., Gerasimenko, N., Marković, S., 2011. An evaluation of geochemical weathering indices in loess-paleosol studies. Quat. Int. 240 (1–2), 12–21. https://doi.org/10.1016/j.quaint.2010.07.019.

Chamberlain, J.A., Westermann, G.E.G., 1976. Hydrodynamic properties of cephalopod shell ornament. Paleobiology 2 (4), 316–331. https://doi.org/10.1017/S0094837300004954.

Chamley, H., 1989. Clay Formation Through Weathering. Clay Sedimentology. Springer, Berlin, Heidelberg, pp. 21–50.

Chamley, H., Pierre, D., 1984. Paleoenvironmental history of the North Atlantic region from mineralogical and geochemical data. Sediment. Geol. 40 (1–3), 151–167. https://doi.org/10.1016/0037-0738(84)90044-7.

Cheel, R.J., Leckie, D.A., Wright, V.P., 1993. Hummocky cross-stratification. Sedimentol. Rev. 1. vol. 1, 103–122.

Chen, P.J., Li, J.J., Matsukawa, M., Zhang, H.C., Wang, Q.F., Lockley, M.G., 2006. Geological ages of dinosaur-track-bearing formations in China. Cretac. Res. 27 (1), 22–32.

Cheng, L.X., 2014. Sedimentary Response within Orogenic Movement of Basin Edge during Late Triassic to Jurassic in Eastern and Northern Sichuan. Chengdu University of Technology (in Chinese), China.

Cohen, A.S., Coe, A.L., Harding, S.M., Schwark, L., 2004. Osmium isotope evidence for the regulation of atmospheric CO_2 by continental weathering. Geology 32 (2), 157–160. https://doi.org/10.1130/G20158.1.

Cullers, R.L., 2002. Implications of elemental concentrations for provenance, redox conditions, and metamorphic studies of shales and limestones near Pueblo, CO, USA. Chem. Geol. 191 (4), 305–327. https://doi.org/10.1016/S0009-2541(02)00133-X.

Cullers, R.L., Podkovyrov, V.N., 2000. Geochemistry of the Mesoproterozoic Lakhanda shales in southeastern Yakutia, Russia: implications for mineralogical and provenance control, and recycling. Precambrian Res. 104 (1–2), 77–93. https://doi.org/10.1016/S0301-9268(00)00090-5.

Cullers, R.L., Basu, A., Suttner, L.J., 1988. Geochemical signature of provenance in sand-size material in soils and stream sediments near the Tobacco Root batholith, Montana, USA. Chem. Geol. 70 (4), 335–348. https://doi.org/10.1016/0009-2541(88)90123-4.

Das, B.K., Al-Mikhlafi, A.S., Kaur, P., 2006. Geochemistry of Mansar Lake sediments, Jammu, India: Implication for source-area weathering, provenance, and tectonic setting. J. Asian Earth Sci. 26 (6), 649–668. https://doi.org/10.1016/j.jseaes.2005.01.005.

Dattilo, B.F., Brett, C.E., Schramm, T.J., 2012. Tempestites in a teapot? Condensation-generated shell beds in the Upper Ordovician, Cincinnati Arch, USA. Palaeogeogr. Palaeoclimatol. Palaeoecol. 367, 44–62. https://doi.org/10.1016/j.palaeo.2012.04.012.

Davies, D.J., Powell, E.N., Stanton, R.J., 1989. Taphonomic signature as a function of environmental process: shells and shell beds in a hurricane-influenced inlet on the Texas coast. Palaeogeogr. Palaeoclimatol. Palaeoecol. 72, 317–356. https://doi.org/10.1016/0031-0182(89)90150-8.

Delpomdor, F., Linnemann, U., Boven, A., Gärtner, A., Travin, A., Blanpied, C., Virgone, A., Jelsma, H., Préat, A., 2013. Depositional age, provenance, and tectonic and paleoclimatic settings of the late Mesoproterozoic-middle Neoproterozoic Mbuji-Mayi Supergroup, Democratic Republic of Congo. Palaeogeogr. Palaeoclimatol. Palaeoecol. 389, 4–34. https://doi.org/10.1016/j.palaeo.2013.06.012.

Dera, G., Pellenard, P., Neige, P., Deconinck, J.F., Pucéat, E., Dommergues, J.L., 2009. Distribution of clay minerals in early Jurassic Peritethyan seas: palaeoclimatic significance inferred from multiproxy comparisons. Palaeogeogr. Palaeocl. 271 (1–2), 39–51. https://doi.org/10.1016/j.palaeo.2008.09.010.

Dera, G., Brigaud, B., Monna, F., Laffont, R., Pucéat, E., Deconinck, J.F., Pellenard, P., Joachimski, M.M., Durlet, C., 2011. Climatic ups and downs in a disturbed Jurassic world. Geology 39 (3), 215–218. https://doi.org/10.1130/G31579.1.

Dessert, C., Dupré, B., Gaillardet, J., François, L.M., Allegre, C.J., 2003. Basalt weathering laws and the impact of basalt weathering on the global carbon cycle. Chem. Geol. 202 (3–4), 257–273. https://doi.org/10.1016/j.chemgeo.2002.10.001.

Dezileau, L., Pizarro, C., Rubio, M.A., 2007. Sequential extraction of iron in marine sediments from the Chilean continental margin. Mar. Geol. 241 (1–4), 111–116. https://doi.org/10.1016/j.margeo.2007.03.006.

Dott Jr., R.H., Bourgeois, J., 1982. Hummocky stratification: significance of its variable bedding sequences. Geol. Soc. Am. Bull. 93 (8), 663–680. https://doi.org/10.1130/0016-7606(1982)93%3C663:HSSOIV%3E2.0.CO;2.

Duke, W.L., 1985. Hummocky cross-stratification, tropical hurricanes, and intense winter storms. Sedimentology 32 (2), 167–194. https://doi.org/10.1111/j.1365-3091.1985.tb00502.x.

Faas, R.W., 1991. Rheological boundaries of mud: where are the limits? Geo-Mar. Lett. 11 (3), 143–146. https://doi.org/10.1007/BF02431000.

Fedo, C.M., Wayne Nesbitt, H., Young, G.M., 1995. Unraveling the effects of potassium metasomatism in sedimentary rocks and paleosols, with implications for

paleoweathering conditions and provenance. Geology 23 (10), 921–924. https://doi.org/10.1130/0091-7613(1995)023<0921:UTEOPM>2.3.CO;2.

Feng, R.C., Wu, Y.Y., Yang, G., Yang, J.J., Liu, M., Zhang, T.S., Yue, T., 2015. Storm Deposition of the Da'anzhai Member (Jurassic) in Central Sichuan Basin. Acta Sedimentol. Sin. 33 (05), 909–918 (in Chinese).

Fick, C., Toldo, E.E., Puhl, E., 2018. Shell concentration dynamics driven by wave motion in flume experiments: Insights for coquina facies from lake-margin settings. Sediment. Geol. 374, 98–114. https://doi.org/10.1016/j.sedgeo.2018.08.002.

Gabet, E.J., Mudd, S.M., 2009. A theoretical model coupling chemical weathering rates with denudation rates. Geology 37 (2), 151–154. https://doi.org/10.1130/G25270A.1.

Gaillardet, J., Dupré, B., Louvat, P., Allegre, C.J., 1999. Global silicate weathering and CO_2 consumption rates deduced from the chemistry of large rivers. Chem. Geol. 159 (1–4), 3–30. https://doi.org/10.1016/S0009-2541(99)00031-5.

Gao, S., Luo, T.C., Zhang, B.R., Zhang, H.F., Han, Y.W., Zhao, Z.D., Hu, Y.K., 1998. Chemical composition of the continental crust as revealed by studies in East China. Geochim. Cosmochim. Ac. 62 (11), 1959–1975. https://doi.org/10.1016/S0016-7037(98)00121-5.

Gao, S.L., Chen, H.H., Dou, W.T., Shao, D.B., Lan, H.B., 1999. Lacustrine Storm Sediment in Yanchang Formation of Ordos Basin. Acta Sedimentol. Sin. 758–762 (in Chinese).

Garzanti, E., Resentini, A., 2016. Provenance control on chemical indices of weathering (Taiwan river sands). Sediment. Geol. 336, 81–95. https://doi.org/10.1016/j.sedgeo.2015.06.013.

Garzanti, E., Padoan, M., Andò, S., Resentini, A., Vezzoli, G., Lustrino, M., 2013a. Weathering and relative durability of detrital minerals in equatorial climate: sand petrology and geochemistry in the East African Rift. J. Geol. 121 (6), 547–580. https://doi.org/10.1086/673259.

Garzanti, E., Padoan, M., Setti, M., Najman, Y., Peruta, L., Villa, I.M., 2013b. Weathering geochemistry and Sr-Nd fingerprints of equatorial upper Nile and Congo muds. Geochem. Geophys. Geosyst. 14 (2), 292–316. https://doi.org/10.1002/ggge.20060.

Garzanti, E., Padoan, M., Setti, M., López-Galindo, A., Villa, I.M., 2014a. Provenance versus weathering control on the composition of tropical river mud (southern Africa). Chem. Geol. 366, 61–74. https://doi.org/10.1016/j.chemgeo.2013.12.016.

Garzanti, E., Vermeesch, P., Padoan, M., Resentini, A., Vezzoli, G., Andò, S., 2014b. Provenance of passive-margin sand (Southern Africa). J. Geol. 122 (1), 17–42. https://doi.org/10.1086/674803.

Godet, A., Bodin, S., Adatte, T., Föllmi, K.B., 2008. Platform-induced clay-mineral fractionation along a northern Tethyan basin-platform transect: implications for the interpretation of Early Cretaceous climate change (Late Hauterivian-Early Aptian). Cretac. Res. 29 (5–6), 830–847. https://doi.org/10.1016/j.cretres.2008.05.028.

Goldberg, K., Humayun, M., 2010. The applicability of the Chemical Index of Alteration as a paleoclimatic indicator: an example from the Permian of the Paraná Basin, Brazil. Palaeogeogr. Palaeocl. 293 (1–2), 175–183. https://doi.org/10.1016/j.palaeo.2010.05.015.

Gould, K.M., Piper, D.J.W., Pe-Piper, G., Andrew MacRae, R., 2014. Facies, provenance and paleoclimate interpretation using spectral gamma logs: application to the Lower Cretaceous of the Scotian Basin. Mar. Pet. Geol. 57, 445–454. https://doi.org/10.1016/j.marpetgeo.2014.06.008.

Guo, Y.L., Yang, S.Y., Su, N., Li, C., Yin, P., Wang, Z.B., 2018. Revisiting the effects of hydrodynamic sorting and sedimentary recycling on chemical weathering indices. Geochim. Cosmochim. Ac. 227, 48–63. https://doi.org/10.1016/j.gca.2018.02.015.

Hallam, A., 1984. Continental humid and arid zones during the Jurassic and cretaceous. Palaeogeogr. Palaeoclimatol. Palaeoecol. 47 (3–4), 195–223. https://doi.org/10.1016/0031-0182(84)90094-4.

Han, Z., Hu, X., Kemp, D.B., Li, J., 2018. Carbonate-platform response to the Toarcian Oceanic Anoxic Event in the southern hemisphere: Implications for climatic change and biotic platform demise. Earth. Planet. Sc. Lett. 489, 59–71. https://doi.org/10.1016/j.epsl.2018.02.017.

Harnois, L., 1988. The CIW index: a new chemical index of weathering. Sediment. Geol. 55 (3), 319–322. https://doi.org/10.1016/0037-0738(88)90137-6.

Hermoso, M., Pellenard, P., 2014. Continental weathering and climatic changes inferred from clay mineralogy and paired carbon isotopes across the early to middle Toarcian in the Paris Basin. Palaeogeogr. Palaeoclimatol. Palaeoecol. 399, 385–393. https://doi.org/10.1016/j.palaeo.2014.02.007.

Hesselbo, S.P., Pieńkowski, G., 2011. Stepwise atmospheric carbon-isotope excursion during the Toarcian Oceanic Anoxic Event (early Jurassic, Polish Basin). Earth Planet. Sci. Lett. 301, 365–372. https://doi.org/10.1016/j.epsl.2010.11.021.

Hesselbo, S.P., Gröcke, D.R., Jenkyns, H., Bjerrum, C.J., Farrimond, P., Morgans Bell, H.S., Green, O.R., 2000. Massive dissociation of gas hydrate during a Jurassic oceanic anoxic event. Nature 406 (6794), 392–395.

Hesselbo, S.P., Jenkyns, H.C., Duarte, L.V., Oliveira, L.C.V., 2007. Carbon-isotope record of the early Jurassic (Toarcian) Oceanic Anoxic Event from fossil wood and marine carbonate (Lusitanian Basin, Portugal). Earth Planet. Sci. Lett. 253 (3–4), 455–470. https://doi.org/10.1016/j.epsl.2006.11.009.

Hill, P.S., Fox, J.M., Crockett, J.S., Curran, K.J., Friedrichs, C.T., Rockwell Geyer, W., Milligan, T.G., Ogston, A.S., Puig, P., Scully, M.E., Traykovski, P.A., Wheatcroft, R. A., 2007. Sediment delivery to the seabed on continental margins. Continent. Margin Sediment. 37, 49–99.

Hu, Z.C., Gao, S., 2008. Upper crustal abundances of trace elements: a revision and update. Chem. Geol. 253 (3–4), 205–221. https://doi.org/10.1016/j.chemgeo.2008.05.010.

Hu, J.M., Zhao, G.C., Meng, Q.R., Luo, H., Wang, Z.H., 2003. The geological features and tectonic significances of the basic swarms in Wudang terrain of Qinling orogen. Acta Petrol. Sin. 19 (4), 601–611 (in Chinese).

Hu, X.M., Li, J., Han, Z., Li, Y.X., 2020. Two types of hyperthermal events in the Mesozoic-Cenozoic: Environmental impacts, biotic effects, and driving mechanisms.

Sci. China Earth Sci. 63, 1041–1058 (in Chinese). https://doi.org/10.1007/s11430-019-9604-4.

Izumi, K., Kemp, D.B., Itamiya, S., Inui, M., 2018. Sedimentary evidence for enhanced hydrological cycling in response to rapid carbon release during the early Toarcian oceanic anoxic event. Earth Planet. Sci. Lett. 481, 162–170. https://doi.org/10.1016/j.epsl.2017.10.030.

Jenkyns, H.C., 1988. The early Toarcian (Jurassic) anoxic event-stratigraphic, sedimentary, and geochemical evidence. Am. J. Sci. 288 (2), 101–151. https://doi.org/10.2475/ajs.288.2.101.

Jennette, D.C., Pryor, W.A., 1993. Cyclic alternation of proximal and distal storm facies: kope and Fairview formations (upper ordovician), Ohio and Kentucky. J. Sediment. Res. 63 (2), 183–203. https://doi.org/10.1306/D4267ABE-2B26-11D7-8648000102C1865D.

Jenny, W.P., 1932. Magnetic Vector study of regional and local geologic structure in principal oil states. AAPG Bull. 16 (12), 1177–1203. https://doi.org/10.1306/3D932AFE-16B1-11D7-8645000102C1865D.

Kamber, B.S., Webb, G.E., 2001. The geochemistry of late Archaean microbial carbonate: implications for ocean chemistry and continental erosion history. Geochim. Cosmochim. Ac. 65 (15), 2509–2525. https://doi.org/10.1016/S0016-7037(01)00613-5.

Kemp, D.B., Selby, D., Izumi, K., 2020. Direct coupling between carbon release and weathering during the Toarcian oceanic anoxic event. Geology 48 (10), 976–980. https://doi.org/10.1130/G47509.1.

Kidwell, S.M., 1986. Models for fossil concentrations: paleobiologic implications. Paleobiology 12 (1), 6–24. https://doi.org/10.1017/S0094837300002943.

Kidwell, S.M., Holland, S.M., 1991. Field description of coarse bioclastic fabrics. Palaios 6, 426–434. https://doi.org/10.2307/3514967.

Kozłowska, A., Poprawa, P., 2004. Diagenesis of the Carboniferous clastic sediments of the Mazowsze region and the northern Lublin region related to their burial and thermal history. Prz. Geol. 52, 491–500.

Kreisa, R.D., 1981. Storm-generated sedimentary structures in subtidal marine facies with examples from the Middle and Upper Ordovician of southwestern Virginia. J. Sediment. Res. 51 (3), 823–848. https://doi.org/10.1306/212F7DBF-2B24-11D7-8648000102C1865D.

Krencker, F.N., Bodin, S., Suan, G., Heimhofer, U., Kabiri, L., Immenhauser, A., 2015. Toarcian extreme warmth led to tropical cyclone intensification. Earth Planet. Sci. Lett. 425, 120–130. https://doi.org/10.1016/j.epsl.2015.06.003.

Lamy, F., Klump, J., Hebbeln, D., Wefer, G., 2000. Late Quaternary rapid climate change in northern Chile. Terra Nova-Oxford. 12 (1), 8–13.

Leonowicz, P., 2011. Sedimentation of Lower Toarcian (Lower Jurassic) brackish deposits from the Częstochowa-Wieluń region (SW Poland). Acta Geol. Pol. 61 (2), 215–241.

Li, C., Yang, S.Y., 2010. Is chemical index of alteration (CIA) a reliable proxy for chemical weathering in global drainage basins? Am. J. Sci. 310 (2), 111–127. https://doi.org/10.2475/02.2010.03.

Li, Y.J., Feng, Y.Y., Liu, H., Zhang, L.H., Zhao, S.X., 2013. Geological characteristics and resource potential of lacustrine shale gas in the Sichuan Basin, SW China. Pet. Explor. Dev. 40 (04), 423–428 (in Chinese).

Li, Y.J., Shao, L.Y., Eriksson, K.A., Tong, X., Gao, C.X., Chen, Z.S., 2014. Linked sequence stratigraphy and tectonics in the Sichuan continental foreland basin, Upper Triassic Xujiahe Formation, Southwest China. J. Asian Earth Sci. 88, 116–136. https://doi.org/10.1016/j.jseaes.2014.02.025.

Liu, S.L., Lin, G., Liu, Y.H., Zhou, Y., Gong, F.X., Yan, Y., 2007. Geochemistry of middle oligocene-pliocene sandstones from the Nanpu Sag, Bohai Bay Basin (Eastern China): implications for provenance, weathering, and tectonic setting. Geochem. J. 41 (5), 359–378. https://doi.org/10.2343/geochemj.41.359.

Liu, J.C., Cao, J., Hu, G., Wang, Y., Yang, R.F., Liao, Z.W., 2020. Water-level and redox fluctuations in a Sichuan Basin lacustrine system coincident with the Toarcian OAE. Palaeogeogr. Palaeoclimatol. Palaeoecol. 58, 1–14. https://doi.org/10.1016/j.palaeo.2020.109942.

Lu, J., Zhou, K., Yang, M.F., Shao, L.Y., 2020. Jurassic continental coal accumulation linked to changes in palaeoclimate and tectonics in a fault-depression superimposed basin, Qaidam Basin, NW China. Geol. J. 55 (12), 7998–8016. https://doi.org/10.1002/gj.3921.

McArthur, J.M., Donovan, D.T., Thirlwall, M.F., Fouke, B.W., Mattey, D., 2000. Strontium isotope profile of the early Toarcian (Jurassic) oceanic anoxic event, the duration of ammonite biozones, and belemnite palaeotemperatures. Earth Planet. Sci. Lett. 179 (2), 269–285. https://doi.org/10.1016/S0012-821X(00)00111-4.

McDonough, W.F., Sun, S.S., 1995. The composition of the Earth. Chem. Geol. 120 (3–4), 223–253. https://doi.org/10.1016/0009-2541(94)00140-4.

McLennan, S.M., Hemming, S., McDaniel, D.K., Hanson, G.N., 1993. Geochemical approaches to sedimentation, provenance, and tectonics. Special Papers-Geol. Soc. Am. 21.

Meunier, A., Caner, L., Hubert, F., El Albani, A., Prêt, D., 2013. The weathering intensity scale (WIS): an alternative approach of the chemical index of alteration (CIA). Am. J. Sci. 313 (2), 113–143. https://doi.org/10.2475/02.2013.03.

Mitchell, J.F.B., 1989. The "greenhouse" effect and climate change. Rev. Geophys. 27 (1), 115–139. https://doi.org/10.1029/RG027i001p00115.

Mongelli, G., Critelli, S., Perri, F., Sonnino, M., Perrone, V., 2006. Sedimentary recycling, provenance and paleoweathering from chemistry and mineralogy of Mesozoic continental redbed mudrocks, Peloritani Mountains, Southern Italy. Geochem. J. 40 (2), 197–209. https://doi.org/10.2343/geochemj.40.197.

Montañez, I.P., Tabor, N.J., Niemeier, D., DiMichele, W.A., Frank, T.D., Fielding, C.R., Isbell, J.L., Birgenheier, L.P., Rygel, M.C., 2007. CO2-forced climate and vegetation instability during late Paleozoic deglaciation. Science 315 (5808), 87–91. https://doi.org/10.1126/science.1134207.

Moore, D.M., Reynolds, R.C., 1997. X-Ray Diffraction and the Identification and Analysis of Clay Minerals. Oxford Univ. Press, New York.

Mulder, T., Chapron, E., 2011. Flood deposits in continental and marine environments: character and significance. Sediment transfer from shelf to deep water—Revisiting the delivery system. AAPG Stud. Geol. 61, 1–30. https://doi.org/10.1306/13271348St613436.

Mulder, T., Migeon, S., Savoye, B., Faugères, J.C., 2001. Inversely graded turbidite sequences in the deep Mediterranean: a record of deposits from flood-generated turbidity currents? Geo-Mar. Lett. 21 (2), 86–93. https://doi.org/10.1007/s003670100071.

Mulder, T., Syvitski, J.P.M., Migeon, S., Faugères, J.C., Savoye, B., 2003. Marine hyperpycnal flows: initiation, behavior and related deposits. A review. Mar. Pet. Geol. 20 (6–8), 861–882. https://doi.org/10.1016/j.marpetgeo.2003.01.003.

Müller, T., Price, G.D., Bajnai, D., Nyerges, A., Kesjár, D., Raucsik, B., Varga, A., Judik, K., Fekete, J., May, Z., Pálfy, J., 2017. New multiproxy record of the Jenkyns Event (also known as the Toarcian Oceanic Anoxic Event) from the Mecsek Mountains (Hungary): differences, duration and drivers. Sedimentology 64 (1), 66–86. https://doi.org/10.1111/sed.12332.

Nesbitt, H.W., Young, G.M., 1982. Early Proterozoic climates and plate motions inferred from major element chemistry of lutites. Nature 299 (5885), 715–717. https://doi.org/10.1038/299715a0.

Nesse, W.D., 2012. Introduction to Mineralogy. Oxford Univ, Press.

Nishida, N., Ito, M., Inoue, A., Inoue, A., Takizawa, S., 2013. Clay fabric of fluid-mud deposits from laboratory and field observations: potential application to the stratigraphic record. Mar. Geol. 337, 1–8. https://doi.org/10.1016/j.margeo.2012.12.006.

Parker, A., 1970. An index of weathering for silicate rocks. Geol. Mag. 107 (6), 501–504. https://doi.org/10.1017/S0016756800058581.

Passey, Q.R., Creaney, S., Kulla, J.B., Moretti, F.J., Stroud, J.D., 1990. A practical model for organic richness from porosity and resistivity logs. AAPG Bull. 74 (12), 1777–1794. https://doi.org/10.1306/0C9B25C9-1710-11D7-8645000102C1865D.

Pattan, J.N., Parthiban, G., Gupta, S.M., Mir, R.A., 2012. Fe speciation and Fe/Al ratio in the sediments of southeastern Arabian Sea as an indicator of climate change. Quat. Int. 250, 19–26. https://doi.org/10.1016/j.quaint.2011.08.007.

Pellenard, P., Deconinck, J.F., 2006. Mineralogical variability of Callovo-Oxfordian clays from the Paris Basin and the Subalpine Basin. Compt. Rendus Geosci. 338 (12−13), 854–866. https://doi.org/10.1016/j.crte.2006.05.008.

Percival, L.M.E., Cohen, A.S., Davies, M.K., Dickson, A.J., Hesselbo, S.P., Jenkyns, H.C., Leng, M.J., Mather, T.A., Storm, M.S., Xu, W.M., 2016. Osmium isotope evidence for two pulses of increased continental weathering linked to early Jurassic volcanism and climate change. Geology 44 (9), 759–762. https://doi.org/10.1130/G37997.1.

Perri, F., 2018. Reconstructing chemical weathering during the lower Mesozoic in the Western-Central Mediterranean area: a review of geochemical proxies. Geol. Mag. 155 (4), 944–954.

Pieńkowski, G., 2004. The epicontinental lower Jurassic of Poland. Polish Geol. Inst. Special Papers 12, 5–154.

Pieńkowski, G., Hodbod, M., Ullmann, C.V., 2016. Fungal decomposition of terrestrial organic matter accelerated early Jurassic climate warming. Sci. Rep. 6 (1), 1–11. https://doi.org/10.1038/srep31930.

Pieńkowski, G., Hesselbo, S.P., Barbacka, M., Leng, M., 2020. Non-marine carbon-isotope stratigraphy of the Triassic-Jurassic transition in the Polish Basin and its relationships to organic carbon preservation, pCO2 and palaeotemperature. Earth-Sci. Rev. 210, 103383.

Puga-Bernabéu, A., Aguirre, J., 2017. Contrasting storm-versus tsunami-related shell beds in shallow-water ramps. Palaeogeogr. Palaeoclimatol. Palaeoecol. 417, 1–14. https://doi.org/10.1016/j.palaeo.2017.01.033.

Robert, C., Kennett, J.P., 1994. Antarctic subtropical humid episode at the Paleocene-Eocene boundary: Clay-mineral evidence. Geology 22 (3), 211–214. https://doi.org/10.1130/0091-7613(1994)022<0211:ASHEAT>2.3.CO;2.

Ruebsam, W., Pieńkowski, G., Schwark, L., 2020. Toarcian climate and carbon cycle perturbations – its impact on sea-level changes, enhanced mobilization and oxidation of fossil organic matter. Earth Planet. Sci. Lett. 546, 116417 https://doi.org/10.1016/j.epsl.2020.116417.

Ruffell, A., Worden, R., 2000. Palaeoclimate analysis using spectral gamma-ray data from the Aptian (Cretaceous) of southern England and southern France. Palaeogeogr. Palaeocl. 155 (3–4), 265–283. https://doi.org/10.1016/S0031-0182(99)00119-4.

Sawyer, E.W., 1986. The influence of source rock type, chemical weathering and sorting on the geochemistry of clastic sediments from the Quetico metasedimentary belt, Superior Province, Canada. Chem. Geol. 55 (1–2), 77–95. https://doi.org/10.1016/0009-2541(86)90129-4.

Sichuan Geology and Mineral Resources Bureau, 1991. Regional Geological Survey of Sichuan Province. Geological Press, Beijing (In Chinese).

Singer, A., 1984. The paleoclimatic interpretation of clay minerals in sediments—a review. Earth-Sci. Re. 21 (4), 251–293. https://doi.org/10.1016/0012-8252(84)90055-2.

Singh, P., 2009. Major, trace and REE geochemistry of the Ganga River sediments: influence of provenance and sedimentary processes. Chem. Geol. 266 (3–4), 242–255. https://doi.org/10.1016/j.chemgeo.2009.06.013.

Slater, S.M., Twitchett, R.J., Danise, S., Vajda, V., 2019. Substantial vegetation response to early Jurassic global warming with impacts on oceanic anoxia. Nat. Geosci. https://doi.org/10.1038/s41561-019-0349-z.

Śródoń, J., 2006. Identification and quantitative analysis of clay minerals. Develop. Clay Sci. 1, 765–787. https://doi.org/10.1016/S1572-4352(05)01028-7.

Stott, P., 2016. How climate change affects extreme weather events. Science 352 (6293), 1517–1518. https://doi.org/10.1126/science.aaf7271.

Suan, G., Mattioli, E., Pittet, B., Mailliot, S., Lécuyer, C., 2008. Evidence for major environmental perturbation prior to and during the Toarcian (early Jurassic) oceanic anoxic event from the Lusitanian Basin, Portugal. Paleoceanography 23 (1). https://doi.org/10.1029/2007PA001459.

Suan, G., Mattioli, E., Pittet, B., Lécuyer, C., Suchéras-Marx, B., Duarte, L.V., Philippe, M., Reggiani, L., Martineau, F., 2010. Secular environmental precursors to early Toarcian (Jurassic) extreme climate changes. Earth Planet. Sci. Lett. 290 (3–4), 448–458. https://doi.org/10.1016/j.epsl.2009.12.047.

Sun, S.S., Dong, D.Z., Li, Y.C., Wang, H.Y., Shi, Z.S., Huang, S.W., Chang, Y., Bai, W.H., 2021. Geological characteristics and controlling factors of hydrocarbon accumulation in terrestrial shale in the Da'anzhai Member of the Jurassic Ziliujing Formation, Sichuan Basin. Oil Gas Geol. 42 (1), 124–135 (in Chinese).

Taylor, S.R., McLennan, S.M., 1985. The Continental Crust: Its Composition and Evolution.

Újvári, G., Varga, A., Raucsik, B., Kovácsb, J., 2014. The Paks loess-paleosol sequence: a record of chemical weathering and provenance for the last 800 ka in the mid-Carpathian Basin. Quat. Int. 319, 22–37. https://doi.org/10.1016/j.sedgeo.2006.05.029.

Vanderaveroet, P., Deconinck, J.-F., 1997. Clay mineralogy of Cenozoic sediments of the Atlantic city Borehole, New Jersey. In: Proceedings of the Ocean Drilling Program, Scientific Results, Vol. 150.

Wang, P., Horwitz, M.H., 2007. Erosional and depositional characteristics of regional overwash deposits caused by multiple hurricanes. Sedimentology 54 (3), 545–564. https://doi.org/10.1111/j.1365-3091.2006.00848.x.

Wang, Y.D., Fu, B.H., Xie, X.P., Huang, Q.S., Jiang, Z.K., 2010. The Terrestrial Triassic and Jurassic Systems in the Sichuan Basin. University of Science & Technology of China Press, China.

Weaver, C.E., 1989. Clays, Muds, and Shales. Elsevier.

West, A.J., Galy, A., Bickle, M., 2005. Tectonic and climatic controls on silicate weathering. Earth Planet. Sci. Lett. 235 (1–2), 211–228. https://doi.org/10.1016/j.epsl.2005.03.020.

White, A.F., Blum, A.E., 1995. Effects of climate on chemical weathering in watersheds. Geochim. Cosmochim. Ac. 59 (9), 1729–1747. https://doi.org/10.1016/0016-7037(95)00078-E.

White, A.F., Blum, A.E., Bullen, T.D., Vivit, D.V., Schulz, M., Fitzpatrick, J., 1999. The effect of temperature on experimental and natural chemical weathering rates of granitoid rocks. Geochim. Cosmochim. Ac. 63 (19v20), 3277–3291. https://doi.org/10.1016/S0016-7037(99)00250-1.

Xia, Z.S., Liu, X.H., Zeng, L.K., Zhou, P.Q., Li, R.N., 1982. Division of late Triassic-old Tertiary continental strata in Sichuan basin. Acta Geol. Sichuan 3 (2), 71 (in Chinese).

Xu, W.M., Ruhl, M., Jenkyns, H.C., Hesselbo, S.P., Riding, J.B., Selby, D., Naafs, B.D.A., Weijers, J.W.H., Pancost, R.D., Tegelaar, E.W., Idiz, E.F., 2017. Carbon sequestration in an expanded lake system during the Toarcian oceanic anoxic event. Nat. Geosci. 10 (2), 129–134. https://doi.org/10.1038/ngeo2871.

Xu, W.M., Ruhl, M., Jenkyns, H.C., Leng, M.J., Huggett, J.M., Minisini, D., Ullmann, C.V., Riding, J.B., Weijers, J.W.H., Storm, M.S., Percival, L.M.E., Tosca, N.J., Idiz, E.F., Tegelaar, E.W., Hesselbo, S.P., 2018. Evolution of the Toarcian (early Jurassic) carbon-cycle and global climatic controls on local sedimentary processes (Cardigan Bay Basin, UK). Earth Planet. Sci. Lett. 484, 396–411. https://doi.org/10.1016/j.epsl.2017.12.037.

Zhou, D.W., Zhang, C.L., Zhou, X.H., Sang, H.Q., 1999. 40Ar/39Ar dating of basic dykes from Wudang block and their geology significance. Acta Petrol. Sin. 15 (1), 14–20 (in Chinese).

Zou, X.W., Duan, Q.F., Tang, C.Y., Cao, L., Cui, S., Zhao, W.Q., Xie, J., Wang, L., 2001. SHRIMP zircon U-Pb dating and lithogeochemical characteristics of diabase from Zhenping area in North Daba Mountain. Geol. China 38 (2), 282–291 (in Chinese).